Multi-foci metalens with polarization-rotated focal points

Xiaofei Zang, Hongzhen Ding, Yuttana Intaravanne, Lin Chen, Yan Peng, Jingya Xie, Qinghong Ke, Alexey. V. Balakin, Alexander. P. Shkurinov, Xianzhong Chen[*], Yiming Zhu[*], Songlin Zhuang

Prof. Xiaofei Zang, Mr. Hongzhen Ding, Prof. Lin Chen, Prof. Yan Peng, Prof. Jingya Xie, Mr. Qinghong Ke, Prof. Alexey. V. Balakin, Prof. Alexander. P. Shkurinov, Prof. YimingZhu, Prof. Songlin Zhuang
Terahertz Technology Innovation Research Institute, and Shanghai Key Lab of Modern Optical System, University of Shanghai for Science and Technology, No. 516 JunGong Road, Shanghai, 200093, China.
E-mail: ymzhu@usst.edu.cn
Mr. Yuttana Intaravanne, Prof. Xianzhong Chen
SUPA, Institute of Photonics and Quantum Sciences, School of Engineering and Physical Sciences, Heriot-Watt University, Edinburgh, EH14 4AS, UK.
E-mail: x.chen@hw.ac.uk
Prof. Alexey. V. Balakin, Prof. Alexander. P. Shkurinov
Department of Physics and International laser Center, Lomonosov Moscow State University, Leninskie Gory 1,Moscow 19991 Russia.
Prof. Alexey. V. Balakin, Prof. Alexander. P. Shkurinov
ILIT RAS – Branch of the FSRC «Crystallography and Photonics» RAS, Svyatoozerskaya 1, 140700, Shatura, Moscow Region, Russia.
((Optional Dedication))

Benefiting from the unprecedented capability of metasurface in the manipulation of light propagation, metalenses can provide novel functions that are very challenging or impossible to achieve with conventional lenses. Here, we propose and experimentally demonstrate an approach to realizing multi-foci metalenses with polarization-rotated focal points based on geometric metasurfaces. Multi-foci metalenses with various polarization rotation directions are developed using silicon pillars with spatially variant orientations. The focusing characteristic and longitudinal polarization-dependent imaging capability are demonstrated upon the illumination of a linearly-polarized light beam. The uniqueness of multi-foci metalens with polarization-rotated focal points may open a new avenue for imaging, sensing, and information processing.

1

1. Introduction

Optical metasurfaces, two-dimensional counterparts of metamaterials, have provided unprecedented capabilities in the modification of light wavefront, enabling a plethora of novel applications such as generalized Snell's law of refraction[1-4], light beam shaping[5-8], Spin-Hall effects[9-12], holograms[13-19], polarization control and analysis[20-22], and nonlinear dynamics[24-27]. In comparison with traditional bulk lenses that rely on the required gradual phase change accomplished by controlling surface profile of the optical material, metalenses are ultrathin and ultraflat, which is desirable for device miniaturization and system integration. As fundamental optical elements, metalenses[29-33] have shown promising applications in imaging, lithography, spectroscopy and laser fabrication due to the ultrathin configuration and ease of fabrication. In addition, metalenses can provide novel functions that are very challenging or impossible to achieve with conventional lenses, which can extend the imaging capability of the current optical systems. Benefiting from the exotic properties of metasurfaces, various types of metalenses with unusual functionalities have been developed. Examples include dual-polarity plasmonic metalens[34], broadband/multispectral achromatic metalens[35-38], metalens array[39], light-sword lens[40], multi-foci lens[41], multifunctional metalens[42] and polarization-dependent metalens[43]. An optical element with polarization manipulation functionality, *i.e.*, polarization rotator, has been used in many research areas ranging from optical isolators[44] to sophisticated organic structure analysis[45]. Thus far, the multi-foci metalens with polarization-controllable functionality has not been demonstrated yet. Unlike previously demonstrated multi-foci lenses[41], we propose and demonstrate a multi-foci metalens with polarization-rotated functionality. Furthermore, although our novel metalens is realized based on the geometric metasurfaces, which are typically spin-dependent (only works for circularly polarized light beams), it can work for linearly-polarized light. The approach is utilized to design terahertz multi-foci lenses with multiple polarization-rotated focal points. As a novel terahertz lens with unusual functionality, the longitudinal polarization-dependent

imaging is experimentally demonstrated. The flexible and robust generation of the polarization-rotated multiple focal spots may find new applications such as polarization-dependent imaging, information detection and displaying.

2. Operating Principle

Figure 1 shows the schematic of a multi-foci metalens with polarization-rotated focal points. Upon the illumination of a linearly-polarized THz beam, the metalens have two focal points, whose polarization directions are rotated in comparison with that of the incident light. Each focal spot with linear polarization can be considered as the superposition of both LCP and RCP components. Therefore, the key to realizing such multi-foci metalens mainly lies in the capability of a single metasuface to simultaneously focus linearly-polarized incident beam and rotate the polarization direction of each focal spot. For simplicity, let us start with a metalens with a single polarization-rotated focal point, which will be extended multiple focal points later. To rotate polarization direction with an angle ϕ, the required transmitted THz fields can be written as

$$\frac{\sqrt{2}}{2}\left\{\frac{\sqrt{2}}{2}\begin{bmatrix}1\\i\end{bmatrix}\exp(-i\phi)+\frac{\sqrt{2}}{2}\begin{bmatrix}1\\-i\end{bmatrix}\exp(i\phi)\right\}, \tag{1}$$

where the incident x-polarized THz beam can be considered as $\begin{bmatrix}1\\0\end{bmatrix}=\frac{\sqrt{2}}{2}\left\{\frac{\sqrt{2}}{2}\begin{bmatrix}1\\i\end{bmatrix}+\frac{\sqrt{2}}{2}\begin{bmatrix}1\\-i\end{bmatrix}\right\}$.

To design a metalens without polarization-rotated functionality, the desired phase profile is governed by

$$\varphi(x,y)=\frac{2\pi}{\lambda}(\sqrt{x^2+y^2+f^2}-|f|), \tag{2}$$

in which λ is the working wavelength and f is the focal length. To combine the polarization rotation and focusing on the metalens, the corresponding Jones vector of transmitted beam can be expressed as follows:

$$\frac{1}{\sqrt{2}}\left\{\frac{1}{\sqrt{2}}\begin{bmatrix}1\\i\end{bmatrix}\exp\left(-i\phi\right)\exp\left(i\varphi(x,y)\right)+\frac{1}{\sqrt{2}}\begin{bmatrix}1\\-i\end{bmatrix}\exp\left(i\phi\right)\exp\left(-i\varphi(x,y)\right)\right\}$$
$$+\frac{1}{\sqrt{2}}\left\{\frac{1}{\sqrt{2}}\begin{bmatrix}1\\i\end{bmatrix}\exp\left(-i\phi\right)\exp\left(-i\varphi(x,y)\right)+\frac{1}{\sqrt{2}}\begin{bmatrix}1\\-i\end{bmatrix}\exp\left(i\phi\right)\exp\left(i\varphi(x,y)\right)\right\}. \tag{3}$$

Since a linearly-polarized light beam can be decomposed into LCP light beam and RCP light beam with same components, a metalens with polarization-rotated functionality can be achieved under the illumination of a linearly-polarized THz beam.

The required phase distribution for metalens is governed by:

$$\Phi(x,y)=\arg\left\{\exp\left[i\left(\phi+\varphi(x,y)\right)\right]+\exp\left[i\left(\phi-\varphi(x,y)\right)\right]\right\}. \tag{4}$$

It should be noticed that the performance of metalens with the target phase profile shown in Eq.4 is implemented purely by geometric phase nanostructures. The target phase in Eq.4 consists of the phase profile of a convex lens (leading to focusing) and a concave lens (resulting in divergent beam). Therefore, under the illumination of LCP THz waves, only half of the transmitted waves will be converted to RCP light (for focusing) with an additional phase delay of ϕ. In contrast, for the RCP incidence, half of the transmitted waves will be converted to LCP light (for focusing) with an additional phase delay of $-\phi$. Under the illumination of linear-polarized light, a linear-polarized focal point with polarization-rotated functionality (with rotating angle of $\pm\phi$) can be realized. The rotation angle of $\pm\phi$ can be realized by rotating all nanostructures with an angle $\pm\phi/2$, resulting in the impart phase delays of $\pm\phi$ and $\mp\phi$ to RCP and LCP components, respectively. Here, only half of the transmitted THz waves converted to RCP/LCP light is attributed to the phase profile of a convex lens $exp(\varphi)$ and a concave lens $exp(-\varphi)$ in Eq.4. Therefore, for the linearly-polarized incidence, the focusing efficiency cannot exceed 50% in theory.

Accordingly, the total phase requirement for a metalens with polarization-rotated focal spots (see schematic of Fig.1) can be described as:

$$\Phi_L(x,y) = \arg\Big\{\exp\big[i(\phi_1 + \varphi_1(x,y))\big] + \exp\big[i(\phi_1 - \varphi_1(x,y))\big]$$
$$+ \exp\big[i(\phi_2 + \varphi_2(x,y))\big] + \exp\big[i(\phi_2 - \varphi_2(x,y))\big]\Big\},$$

(5)

where φ_1, φ_2 are the two phase profiles for the generation of two separate focal points, whose corresponding rotation angles of polarization are represented by ϕ_1 and ϕ_2, respectively. Although both φ_1 and φ_2 are designed based on Eq. (2), the two focal lengths f_1 and f_2 are different. The rotation angles of these two longitudinally distributed focal spots can be same ($\phi_1 = \phi_2 \neq 0$) or different ($\phi_1 \neq \phi_2$). As a consequence, the polarization rotation and focal lengths of the multi-foci metalens can be flexibly modulated with various combinations of ϕ_1, ϕ_2 and φ_1, φ_2. The design details of the proposed multi-foci metalens with polarization rotated focal spots are given in Supplementary Materials Section 1. The numerical simulation of polarization-independent focusing is provided in Supplementary Materials Section 2.

3. Results

The dielectric metasurface consisting of anisotropic silicon micro-pillars with spatially variant orientations sitting the silicon substrate is used to simultaneously realize lens focusing and polarization rotation, as shown in Fig. 2(a). Each micro-pillar in the metasurface can be considered as a half-wave plate, which can rotate the polarization or focusing by an abrupt phase (Pancharatnam-Berry phase) delay of $\pm 2\theta$, where θ is the angle between the long side of micro-pillar and x-axis, and the sign of the phase is determined by the helicity of the incident light beam(LCP or RCP). The length, width, and height of each micro-pillar are optimized as L=85 μm, W=40 μm, and H=500 μm, respectively, and the pixel size is P=110 μm along both x-axis and y-axis (The design of the silicon pillars is shown in Supplementary Materials Section 3). Figures 2(b)～2(d) show the optical images of the fabricated metalens to generate single focal spot, longitudinal multiple focal spots, and transversal multiple focal spots, respectively. To characterize the performance of these unusual THz metalenses and

polarization-dependent imaging, near-field scanning terahertz microscopy (NSTM) is utilized to detect the corresponding field distributions (see schematic of the experimental setup in Fig. 2(e)). A laser beam with λ=780 nm is splitted into two parts: one part of the beam is coupled onto the THz tip for detecting the field distributions, while the other part is shined on the photoconductive antenna to generate the THz waves. The THz tip is located in front of the sample to record the electric field distributions of focal points and imaging, while the position of the metalens is fixed. The measurement method is also shown in Experimental Section.

As a feasibility study, a metalens with a single polarization-rotated focal point is initially demonstrated. Such a metalens (see Fig. 2(b)) consists of 100×100 micro-pillars (with the corresponding side length of 11.0 mm), and the working frequency is 0.69 THz. The structure parameters in Eq. (4) are as follows: f=6mm (focal length) and $\phi = 90^0$ (polarization rotating angle). Figure 3 shows the numerical simulation and experimental results of this metalens. The finite difference time domain method is used to calculate the field distribution after the incident light passes through such metalens at normal incidence. For a linearly-polarized incident THz beam with polarization along x-axis (x-polarized), one focal spot is clearly observed at z=6mm away from the surface of metalens, as shown in Fig. 3(a). It should be noted that the polarization axis of the incident light is rotated by 90^0 at the focal point. The x-polarized electric field distribution ($|E_x|^2$) of such metalens is also calculated, as shown in Fig. 3(b). It can be seen that none of the x-polarized electric field contributes to the focal spot, unambiguously demonstrating the polarization rotation of the converted THz beam (focal spot). The numerical calculations agree well with the theoretical design parameters of f=6mm and $\phi = 90^0$. The experimental results are shown in Figs. 3(c) and 3(d). A linearly-polarized (LP) THz beam along the x-axis is focused into a focal spot away from the sample surface (nearby z=6mm), and the polarization axis is rotated by an angle of 90^0, generating a y-polarized focal spot. Both the experimental results and numerical simulations agree well with

each other, except for a slight discrepancy, which can be attributed to the sample imperfection and the limited number of micro-pillars in metalens. The electric field distributions in *x-y* plane ($|E_x|^2$ and $|E_y|^2$) are also given in Figs. 3(e)～3(h). At the real focal plane *z*=6mm, a focal spot with polarization rotation of $\frac{\pi}{2}$ is observed, as shown in Figs. 3(e) and 3(g), respectively, while none of the *x*-polarized focal spot is observed (see Figs. 3(f) and 3(h)). The schematic that represents the characteristic of such metalens and the corresponding electric field distributions in *y-z* plane are given in Supplementary Materials Section 4.

Nevertheless, a single device with more functions, *i.e.*, multiple focal spots with functionality of polarization rotation (see Fig.4), is desirable for device miniaturization and system integration. Inspired by this, we further design a longitudinal polarization-rotatable multi-foci metalens (see schematic of Fig.1 and sample of Fig. 2(c)). According to Eq. (5), we design such a metalens with structure parameters of f_1=3mm (focal length of the first focal spot), f_2=6mm (focal length of the second focal spot), $\phi_1 = 90^0$ (rotation angle of polarization for left focal spot) and $\phi_2 = 0^0$ (non-polarization-rotation for the right focal spot). Under the illumination of *x*-polarized THz waves at 0.69 THz, a focal spot located at *z*=3mm with polarization along *y*-axis is achieved, as shown in Fig. 4(a). In contrast, an *x*-polarized focal spot is observed at *z*=6mm (see Fig. 4(b)). Figures 4(c) and 4(d) show the measured results, in which there are also two linearly-polarized focal spots with orthogonal polarizations at *z*=3mm and *z*=6mm, respectively. Good agreement between the experimental results and theoretical prediction is observed, confirming the properties of multiple focal spots and polarization rotation. Figures 4(e)～4(h) show the corresponding electric distributions in *x-y* plane. The two-dimensional field distributions also demonstrate the above characteristics. The calculations and measurements of the field distributions in *y-z* and *x-y* planes are also supplied in Supplementary Materials Section 5.

Our design principle can not only steer THz beam to form multiple focal spots in longitudinal direction, but also enable the ability to harness the THz waves in transverse direction, leading to the transversal multiple focal points (see the principle of transversal multiple focal spots given in Supplementary Materials Section 1.). Figure 5(a) shows the schematic of proposed metalens that can split a linearly-polarized THz beam into two LP focal spots in ±x-axis without polarization rotation. The required phase distribution for such metalens is expressed as:

$$\Phi_T(x,y) = \arg\left\{ \exp\left[i\left(\phi+\varphi(x,y)+\delta_x\right)\right] + \exp\left[i\left(\phi+\varphi(x,y)-\delta_x\right)\right] \right. \\ \left. + \exp\left[i\left(\phi-\varphi(x,y)+\delta_x\right)\right] + \exp\left[i\left(\phi-\varphi(x,y)-\delta_x\right)\right] \right\},$$

(6)

where $\delta_x = (\pi/7)$ is the phase gradient in x-axis, and the polarization rotating angle is 0 ($\phi=0$, non-polarization rotation). Figures 5(b) and 5(c) show the numerical results for the transversal multiple focal spots. Under the illumination of x-polarized THz waves, it is splitted and focused into two spots in transverse direction (±x-axis), and the polarization of each spot is parallel to the incident THz waves. The experimental demonstrations of beam splitters with functionality of focusing are given in Figs. 5(d) and 5(e), respectively. As illustrated in Fig. 5(f)～5(i), the electric field distributions in x-y plane also reveal the function of our designed metalens. In addition, the transversal polarization-rotated multi-foci metalens is demonstrated in Supplementary Materials Section 6.

4. Discussion

To simultaneously characterize the lens imaging functionality and polarization rotation capability, a polarization-dependent sample is designed, as shown in Fig. 6(a). As a proof-of-concept, we utilize longitudinal multi-foci metalens to realize THz polarization-dependent imaging. Although terahertz imaging[46,47] and tomography[48], that are scanning imaging, have been successfully applied in the areas of nondestructive testing, such as pattern recognition

and bio-imaging, the polarization-dependent imaging (for the polarization-dependent pattern) has not been demonstrated yet. Here, a Chinese character of "Sun" consisting of two symmetrically placed capital letters "E" is fabricated. Each capital letter is composed of periodic arranged metal slits coating on the PI (polyimide) film, in which the slit for the left "E" is parallel to y-axis while it is perpendicular to y-axis for the right "∃", as shown in Fig. 6(b). The numerical simulations of transmitting characteristics for the metal slit are shown in the Supplementary Materials Section 7. The calculations for polarization-dependent imaging are shown in Figs. 6(c) and 6(d). For the illumination of y-polarized THz waves, the left pattern of "E" is revealed, and the right "∃" is not observed (see Fig. 6(c)). In this case, the incident THz waves is almost fully reflected on the left "E", and nearly perfectly transmitted on the right "∃" and surroundings, resulting in the pattern of "E". In contrast, for the x-polarized illumination, the right "∃" is observed. In our experiment, the location of the detector (THz tip) and metalens is fixed while the polarization-sensitive sample (embedded in the left or right focal spot) is scanning/shifting to reveal the desired pattern. As shown in Figs. 6(e) and 6(f), we observe two symmetrically placed capital letters "E" revealed from two polarization-orthogonal focal spots, demonstrating the properties of the multi-foci metalens with polarization-rotated focal points.

High temperature gas-cooled reactor (HTGR), as the next generation nuclear plant (NGNP), is entirely dependent on the large graphite core [49]. Irradiation creep, one crucial property of the nuclear graphite, is the tendency of graphite to deform permanently (or slowly move) due to the influence of radiation and temperature [502]. The irradiation creep of graphite may become very large, and inevitably degrades its function under certain reactor conditions. Therefore, how to monitor the irradiation creep of graphite is critical important for HTGR. Terahertz polarization-dependent imaging of nuclear graphite is one of the most advanced approaches to detect the irradiation creep, since it is a non-destructive evaluation technique to monitor mechanical properties of graphite [51]. Our approach can be extended to design

multiple focal spots (more than two focal points) with arbitrary polarization rotation directions. Therefore, it can be practically applied into the polarization-dependent imaging of nuclear graphite for detecting the irradiation creep of graphite.

Polarization conversion efficiency plays an important role in the evaluation of device performance. In this work, the polarization conversion efficiency is defined as the ratio between the power of desired polarization rotation and incident power, similar to that in Ref [52]. The polarization conversion efficiency for the micro-pillars with same orientations at 0.69 THz is 97% in the simulation. The detailed discussion of the simulated and measured polarization conversion efficiency and focusing efficiency (for simulations) are provided in Supplementary Materials Section 8.

The approach can be used to design geometric metasurface with simultaneous control of the phase and polarization in all spatial dimensions, which can enable the capability to realize efficient functional THz multi-foci metalens with applications in polarization-dependent imaging. Inspired by device miniaturization and system integration, the longitudinal and transversal multi-focal metalens with functionality of polarization-manipulation are designed and experimentally demonstrated. In our work, the uniqueness of the proposed THz metalens is the integration of different functionalities, *i.e.*, longitudinal multiple focal spots with different polarizations, leading to the simultaneous multiplexing of focusing and polarization rotation in a single device. On the other hand, such polarization-rotated multi-foci metalens is directly applied for THz polarization-dependent imaging, which has not been demonstrated yet. Unlike the traditional metalens that were applied in diverse types of imaging such as magnified and demagnified imaging, achromatic imaging, and full-color light-field imaging, the polarization-dependent multi-foci metalens were designed for realizing multiple images that were revealed depending on the polarization. Our unique design will enable the metalens with unusual functions that are very difficult or impossible to achieve with conventional lenses.

5. Conclusion

In summary, we have proposed and demonstrated an approach to develop metalens with multiple polarization-rotated focal spots. The polarization axis of the incident linearly polarized light beam is rotated at each focal point. The longitudinal and transversal multiple focal spots with predesigned polarization rotation are experimentally demonstrated. Benefiting from unique property of the metalens, THz polarization-dependent imaging is demonstrated. The simplicity and robustness of our design not only provide a platform for simultaneous multiplexing of focusing and polarization rotation, but also open a novel avenue for polarization-dependent imaging.

6. Experimental section

Sample fabrication: We use a 1000-μm-thick intrinsic silicon wafer (<100>, Ω =10000 ohm) for the fabrication of the metalens. The AZP4620 photoresist (with thickness of $7\sim8$ μm) is spun (with spin speed of 6000 RPM) onto the silicon wafers cleaned in ultrasonic bath. Then, the photoresist film is baked at 100ºC on a hotplate for 1 minute. A mask aligner (IMP SF-100) is used for the exposure of the resist film. After the development process, the resist film with micro-pillars is baked at 100ºC for 2 minutes and then etched using the DRIE (Bosch) process with SF_6 and C_4F_8 for 95 minutes. Finally, the silicon micro-pillars are obtained after the photoresist is removed by using acetone. For the imaging sample, the photoresist is spin-coated on one side of the PI film, and the mask is utilized for exposure processing. The gold array (imaging sample) is formed after metal coating and ultrasonic stripping.

Experimental setup: The near-field scanning terahertz microscopy (NSTM)[53,54], as illustrated in Fig. 2(e), is built up to perform the characterization of the fabricated samples. A femtosecond laser is used to generate a laser beam with a wavelength of 780 nm, which is splitted into two parts. One part of the light is guided into the photoconductive antenna emitter to generate THz waves, and the THz beam impinges on the metalens (and imaging sample). The other part is coupled into a single-mode fiber with length of 10 cm, and then shines on the THz tip/detector for detecting the electric field distributions. The THz tip is mounted on a three-dimensional translation stage, enabling the capability of 3D field scanning. The position of the metalens is fixed and the THz tip is inside the focusing region to scan the

field distribution. The electric field is detected with a step size of 25 μm along both *x*-direction and *y*-direction and 100 μm step size along *z*-direction. For the polarization-dependent imaging, the position of the metalens and THz tip is fixed while the imaging sample is moved step-by-step for imaging with a step size of 200 μm along both *x*-direction and *y*-direction.

Author Contributions

X.Z., X.C. and Y.Z. initiated the idea. H. D. and X.Z. conducted the numerical simulations. H. D. and X.Z. performed the measurements. X.Z., H. D. Y. I. L. C. Y. P. J. X. Q. K. A. B. A. S. X. C. Y. Z.and S. Z. prepared the manuscript. X.Z., X.C. and Y.Z. supervised the project. All the authors discussed and analysed the results.

Supporting Information

Supporting Information is available from the Wiley Online Library or from the author.

Acknowledgements

References

[1] N. F. Yu, P. Genevet, M. A. Kats, F. Aieta, J. P. Tetienne, F. Capasso, Z. Gaburro. *Science* **2011**, *334*, 333.

[2] L. Huang, X. Chen, H. Mühlenbernd, G. Li, B. Bai, Q. Tan, G. Jin, T. Zentgraf, S. Zhang. *Nano Lett.* **2012**, *12*, 5750.

[3] X. Ni, N. K. Emani, A. V. Kildishev, A. Boltasseva, V. M. Shalaev. *Science* **2012**, *335*, 427.

[4] X. Luo. Sci. China: Phys., Mech. Astron. **2012,** *58,* 594201.

[5] B. Walther, C. Helgert, C. Rockstuhl, F. Setzpfandt, F. Eilenberger, E. Kley, F. Lederer, A. Tunnermann, T. Pertsch. *Adv. Mater.* **2012**, 24, 6300.

[6] X. Chen, Y.Zhang, L. Huang, S. Zhang. *Adv. Opt. Mater.* **2014**, 2, 978.

[7]H. Liu, M. Mehmood, K. Huang, L. Ke, H. Ye, P. Genevet, M. Zhang, A. Danner, S. Yeo, C. Qiu, J. Teng. *Adv. Opt. Mater.* **2014**, 2, 1193.

[8] X. Yin, Z. Ye, J. Rho, Y. Wang, X. Zhang, *Science* **2013**, *339*, 1405.

[9] M. Pu, X. Li, X. Ma, Y. Wang, Z. Zhao, C. Wang, C. Hu, P. Gao, C. Huang, H. Ren, X. Li, F.Qin, J. Yang, M. Gu, M. Hong, X. Luo. *Sci. Adv.* **2015,** 1, e1500396.

[10] X. Ling, X.Zhou, X. Yi, W. Shu, Y.Liu, S. Chen, H. Luo, S.Wen, D. Fan. *Light: Sci & Appl.* **2014**, 4, e290.

[11] W. Luo, S. Xiao, Q. He, S. Sun, L. Zhou. *Adv. Opt. Mater.* **2015**, 3, 1102.

[12]J. Zhou, H. Qian, G. Hu, H. Luo, S. Wen, Z. Liu. *ACS Nano* **2018**, 12, 82.

[13]G. Zheng, H. Mühlenbernd, M. Kenney, G. Li, T. Zentgraf, S. Zhang. *Nat Nanotechnol*. **2015**, *10*, 308.

[14]Y. W. Huang, W. T. Chen, W. Tsai, P. Wu, C. Wang, G. Sun, D. P. Tsai. *Nano. Lett.* **2015**, *15*, 3122.

[15]D. Wen, D. F. Yue, G. Li, G. Zheng, K. Chan, S. Chen, M. Chen, K. F. Li, P. W. H. Wong, K. W. Cheah, E. Y. B. Pun, S. Zhang, X. Chen. *Nat. Commun.* **2015**, *6*, 8241.

[16]B. Wang, F. Dong, Q. T. Li, D. Yang, C. Sun, J. Chen, Z. Song, L. Xu, W. Chu, Y. F. Xiao, Q. Gong, Y. Li. *Nano. Lett.* **2016***, 16*, 5235.

[17]X. Li, L. Chen, Y. Li, X. Zhang, M. Pu, Z. Zhao, X. Ma, Y. Wang, M. Hong, X. Luo. *Sci. Adv.* **2016**, *2*, e1601102.

[18]L. Jin, Z. Dong, S. Mei, Y. Yu, Z. Wei, Z. Pan, S. Rezaei, X. Li, A. Kuznetsov, Y. Kivshar, J. Yang, C. Qiu. *Nano Lett.* **2018**, 18, 8016.

[19]Y.Chen, J. Gao, X. Yang. *Light: Sci & Appl.* **2018**, 7, 84.

[20]N. K. Grady, J. E. Heyes, D. R. Chowdhury, Y. Zeng, M. T. Reiten, A. K. Azad, A. J. Taylor, D. A. R. Dalvit, H. T. Chen. *Science* **2013**, *340*, 1304.

[21]L. Cong, N.Xu, J. Gu, R.Singh, J. Han, W. Zhang. *Laser & Photon. Rev.* **2014**, 8, 626.

[22]R. Fan, Y. Zhou, X. Ren, R.Peng, S. Jiang, D. Xu, X. Xiong, X.Huang, M. Wang. *Adv. Mater.* **2015**, 27, 1201.

[23]P. Wu, W. Tsai, W. Chen, Y. Huang, T. Chen, J. Chen, C. Liao, C. Chu, G. Sun, D. Tsai. *Nano Lett.* **2017**, 17, 445.

[24]G. Li, S. Chen, N. Pholchai, B. Reineke, P. Won, E. Pun, K. Cheah, T.Zentgraf. S. Zhang. *Nat. Mater.* **2015**. 14, 607.

[25]E. Almeida, G. Shalem, Y. Prior. *Nat. Commun.* **2016**, 7, 10367.

[26]W. Ye, F. Zeuner, X. Li, B. Reineke, S. He, C. Qiu, J. Liu, Y. Wang, S. Zhang, T. Zentgraf. *Nat. Commun.* **2016**, 7, 11930.

[27]F. Walter, G. Li, C. Meier, S. Zhang, T. Zentgraf. *Nano Lett.* **2017**, 17, 3171.

[28]D. Hu, X. Wang, S. Feng, J. Ye, W. Sun, Q. Kan, P. Klar, Y. Zhang. *Adv. Opt. Mater.* **2013**, 1, 186.

[29]D. Lin, P. Fan, E. Hasman, M. Brongersma. *Science* **2014**, 345, 298.

[30]M. Khorasaninejad, W. Chen, R. Devlin, J. Oh, A. Zhu, F. Capasso. *Science* **2016**, 353, 1190.

[31]M. Khorasaninejad, W. Chen, A. Zhu, R. Devlin, J. Oh, F. Capasso. *Nano Lett*. **2016**, 16, 4595.

[32]B.Chen, P. Wu, V. Sun, Y. Lai, C. Chu, I. Lee, J. Chen, Y. Chen, Y. Lan, C. Huang, D. Tsai. *Nano Lett.* **2017**, 17, 6345.

[33]C. Schlickriede, N. Waterman, B. Reineke, P. Georgi, G. Li, S. Zhang, T. Zentgraf. *Adv. Mater.* **2018**, 30, 1703843.

[34]X. Chen, L. Huang, H. Mühlenbernd, G. Li, B. Bai, Q. Tan, G. Jin, C. Qiu, S. Zhang, T. Zentgraf. *Nat. Commun.* **2012**, *3*, 1198.

[35]A. Arbabi, Y. Horie, A. Ball, A. Faraon. *Nat. Commun.* **2015**, 6, 7069.

[36]R. Panigua-Dominguez, Y. Yu, E. Khaidarov, S. Choi, V. Leong, R. Bakker, X. Liang, Y. Fu, V. Valuckas, L. Krivitsky. *Nano Lett.* **2018**, 18, 2124.

[37]S. M. Wang, P. C. Wu, V.-C. Su, Y.-C. Lai, C. H. Chu, J.-W. Chen, S.-H. Lu, J. Chen, B. B. Xu, C.-H. Kuan, T. Li, S. N. Zhu, and D. P. Tsai, *Nat. Commun.* **2017**, *8*, 187.

[38]Z. Zhao, M. Pu, H. Gao, J. Jin, X. Li, X. Ma, Y. Wang, P.Gao, X. Luo. *Sci. Rep.* **2015,** 5, 15781.

[39]R. Lin, V. Sun, S. Wang, M. Chen, T. Chung, Y.Chen, H. Kuo, J. Chen, J. Chen, Y. Huang, J. Wang, C. Chu, P. Wu, T. Li, Z. Wang, S. Zhu, D. Tsai. *Nat. Nano.* **2019**, 14, 227.

[40]Z. Zhang, D. Wen, C. Zhang, M. Chen, W. Wang, S. Chen, X. Chen. *ACS Photon*. **2018**, 5, 1794.

[41]X. Chen, M. Chen, M. Mehmood, D. Wen, F. Yu, C. Qiu, S. Zhang. *Adv. Opt. Mater.* **2015**, 3, 1201.

[42]D. Wen, F. Yue, M. Chen, X. Chen. *Sci. Rep.* **2016**, 6, 27628.

[43]A. Arbabi, Y. Horie, M. Bagheri, A. Faraon. *Nature Natecnnol.* **2015**, 10, 937.

[44]A. Shaltout, J. Liu, V. Shalaev, A. Kildishev. Optically active metasurface with non-chiral plasmonic nanoantennas. *Nano Lett.* **2014**, 14, 4426.

[45]D. Kovtun, I. Kochikov, Y. Tarasov. *J. Mol. Struct.* 2015, 100, 311.

[46]M. Schirmer, M. Fujio, M. Minami, J. Miura, T. Araki, T. Yasui. *Bio. Opt. Express* **2010**, 1, 354.

[47]J. Wang, R. Stantchev, Q. Sun, T. Chiu, A. Ahuja, E. Pickwell-Macpherson. *Bio. Opt. Express* **2018**, 9, 6467.

[48]D. Suzuki, S. Oda, Y. Yawano. *Nat. Photon.***2016**, 10, 809.

[49]W. Windes, T. Burchell, M. Carroll, *Idaho National Laboratory*, 2010.

[50]T. D. Burchell. J. Nuc. Mater. **2008**, 381, 46.

[51]J. Zhang, A. Redo-Sanchez, X. C. Zhang, *Fron. Opt.* 2012.

[52]X. Zang, F. Dong, F. Yue, C. Zhang, L. Xu, Z. Song, M. Chen, P. Chen, G. S. Buller, Y. Zhu, S. Zhuang, W. Chu, S. Zhang, X. Chen. *Adv. .Mater.* **2018**, 30, 1707499.

[53]L. Chen, Y. Wei, X. Zang, Y. Zhu, and S. Zhuang, *Sci. Rep.* **2016,** 6, 22027.

[54] L. Chen, D. Liao, X. Guo, J. Zhao, Y. Zhu and S. Zhuang, *Front. Inform. Tech. & EL*, **2019,** 20, 591.
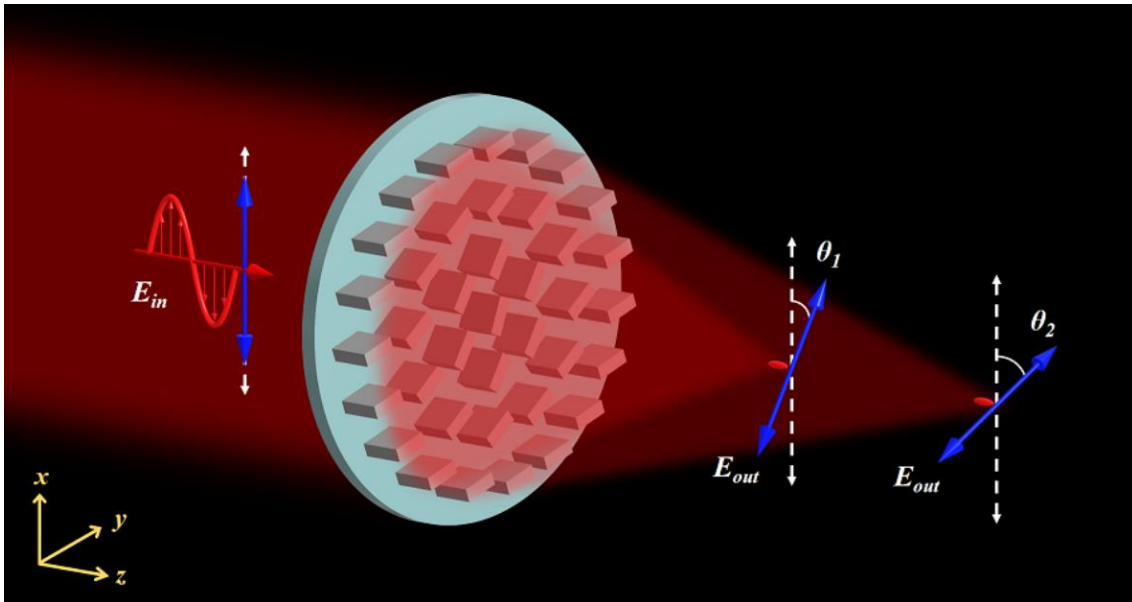
Fig.1. Schematic of the multi-foci metalens with polarization-rotated focal points. Under the illumination of linearly-polarized THz waves, two longitudinally distributed focal spots. The polarization axis of the incident linearly-polarized light beam is rotated at each focal point. The two polarization rotated angles are θ_1 and θ_2, respectively.
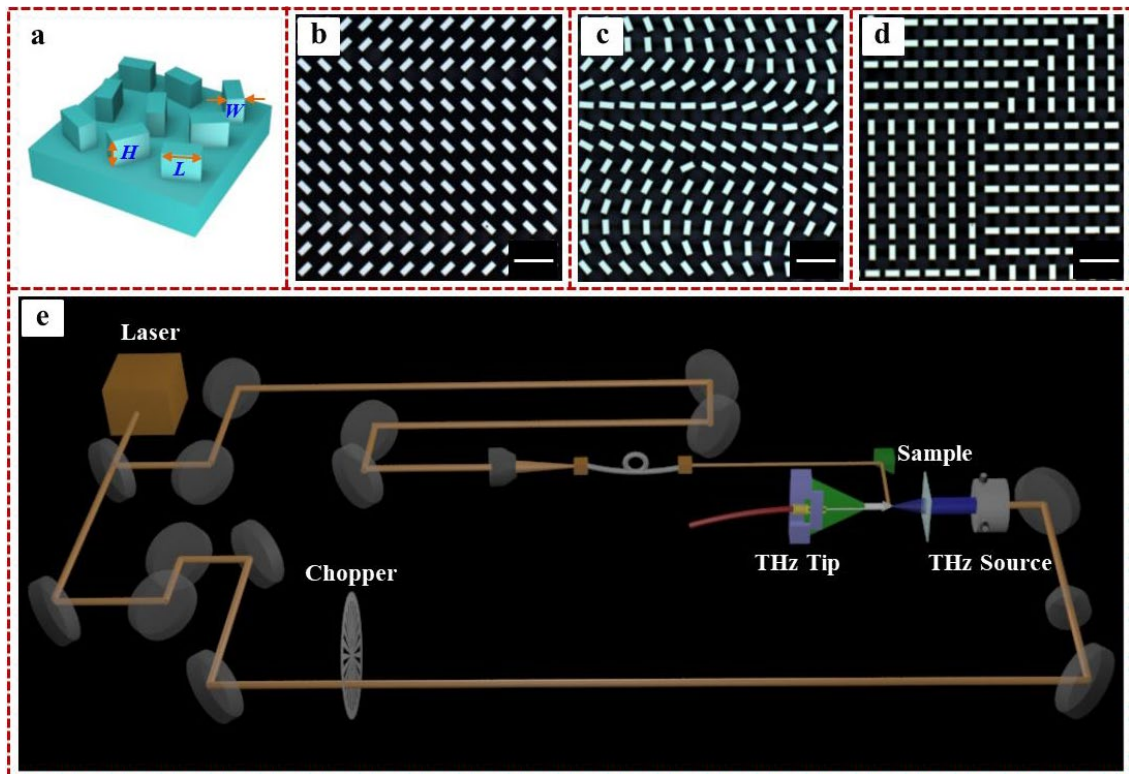
Fig.2. Design and fabrication of the metasurface and schematic of the experimental setup. a Schematic of the designed metasurface with silicon-based micro-pillars sitting on a silicon substrate. **b ~ d** The optical images of the fabricated metalenses to generate polarization-rotated single focal point, longitudinal multiple focal points, and transversal multiple focal points, respectively. The scale bar in the figures is 200μm. **e** Schematic of the experimental setup to characterize the properties of the metalens and polarization-dependent imaging. All of the designed metalenses consists of 100×100 micro-pillars, meaning that they are square, not circular. The side length of the square is 11.0mm.
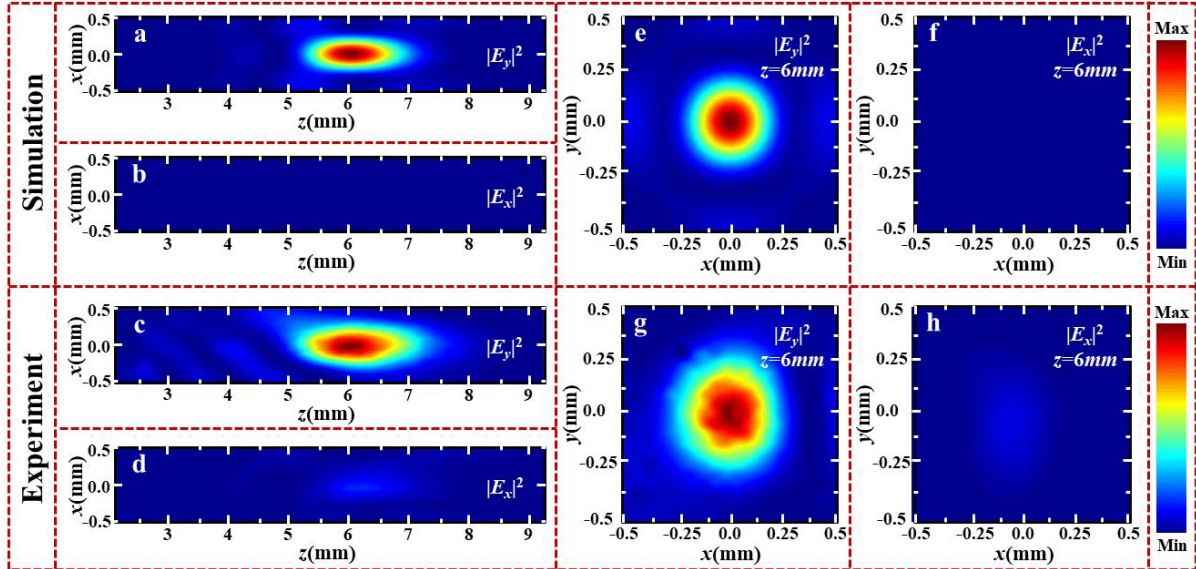
Fig.3. Electric field distributions for the metalens with a single polarization-rotated focal point. a and **b** The simulated *y*- and *x*-polarized electric field distributions for the transmitted THz waves at *x-z* plane under the illumination of *x*-polarized THz waves. **c** and **d** The corresponding experimental results. **e** and **f** The simulated electric field distributions for the designed metalens at *x-y* plane and *z*=6mm. **g** and **h** The corresponding measurements for the designed metalens at *x-y* plane and *z*=6mm.
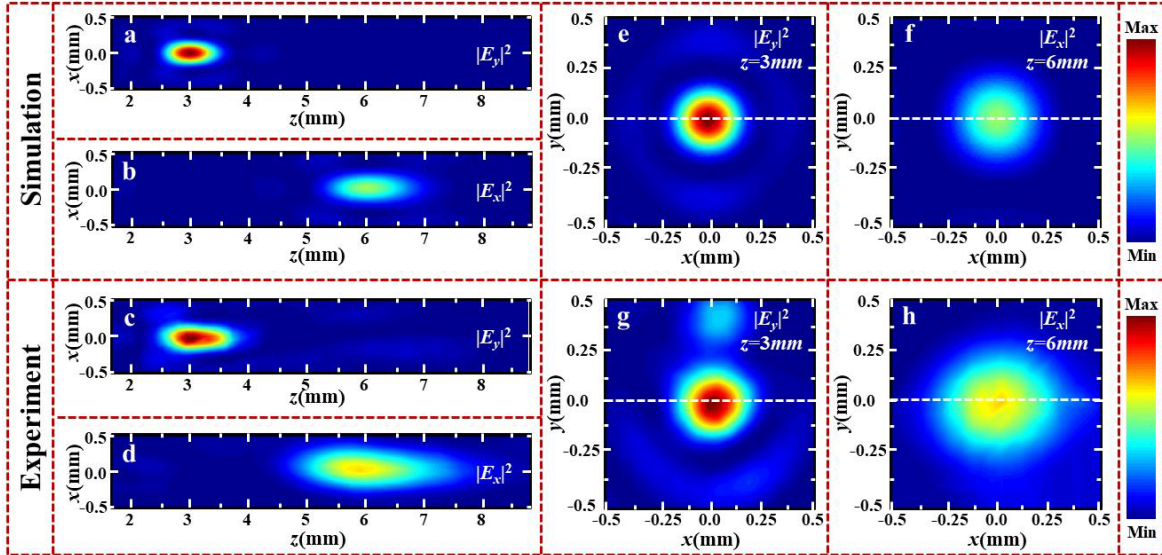
Fig.4. Electric field distributions for the metalens with polarization-rotated longitudinal multi-foci metalens. a and **b** The simulated *y*- and *x*-polarized electric field distributions for the transmitted THz waves at *x-z* plane under the illumination of *x*-polarized THz waves. **c** and **d** The corresponding measurments. **e** and **f** The simulated electric field distributions for the designed metalens at *x-y* plane and *z*=3mm, *z*=6mm, respectively. **g** and **h** The corresponding measurments for the designed metalens at *x-y* plane and *z*=3mm, *z*=6mm, respectively.
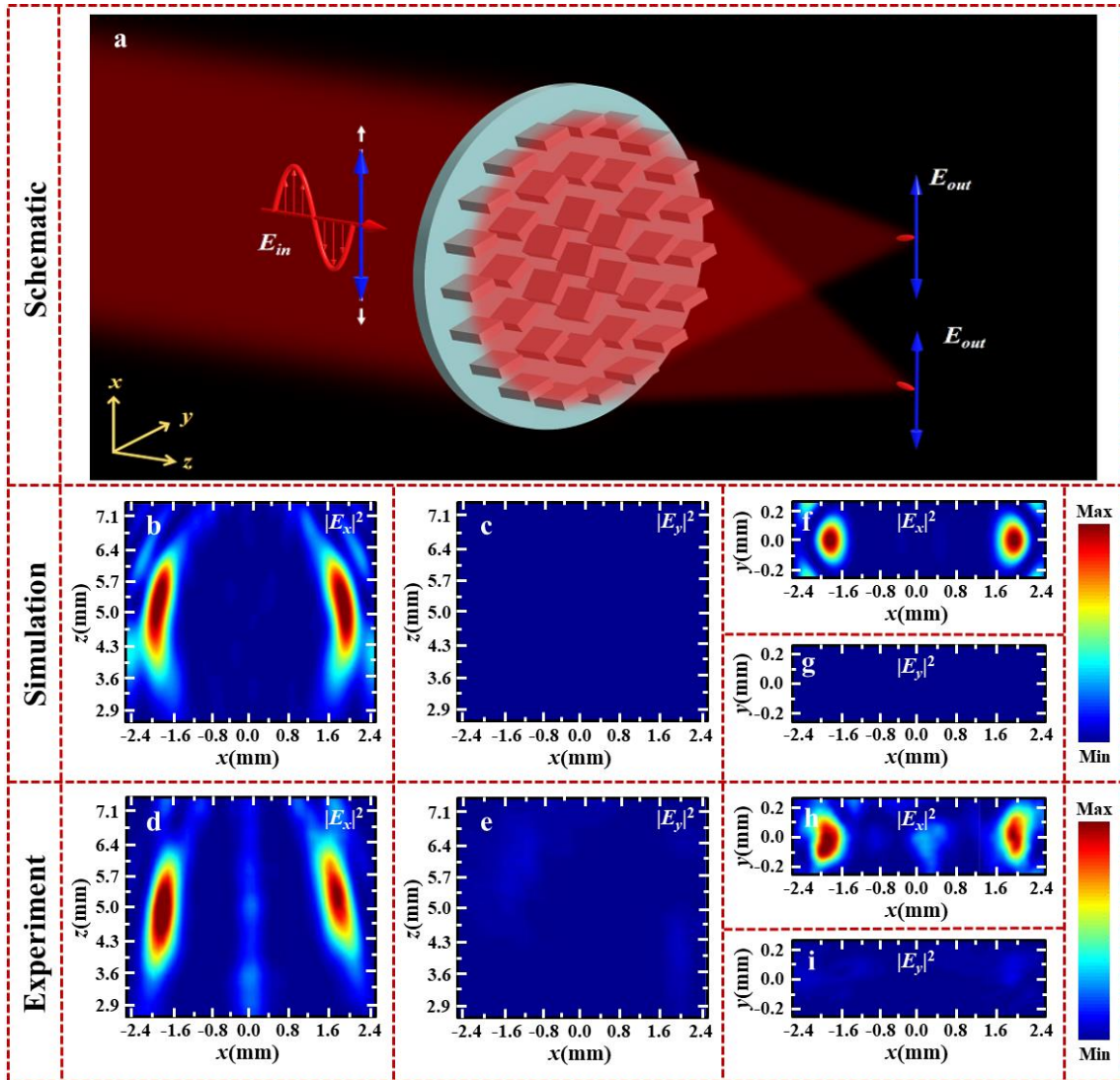
Fig.5. Schematic and electric field distributions for the transverse multi-foci metalens. a The schematic for the transverse dual-foci metalens under the illumination of *x*-polarized THz waves. **b** and **c** The simulated *x*- and *y*-polarized electric field distributions for the transmitted THz waves at *x-z* plane. **d** and **e** The corresponding measurements for the metalens with polarization-rotated transverse dual-foci metalens. **f** and **g** The simulated electric field distributions for the designed metalens at *x-y* plane and *z*=5mm, respectively. **h** and **i** The corresponding measurments for the designed metalens at *x-y* plane and *z*=5mm, respectively.
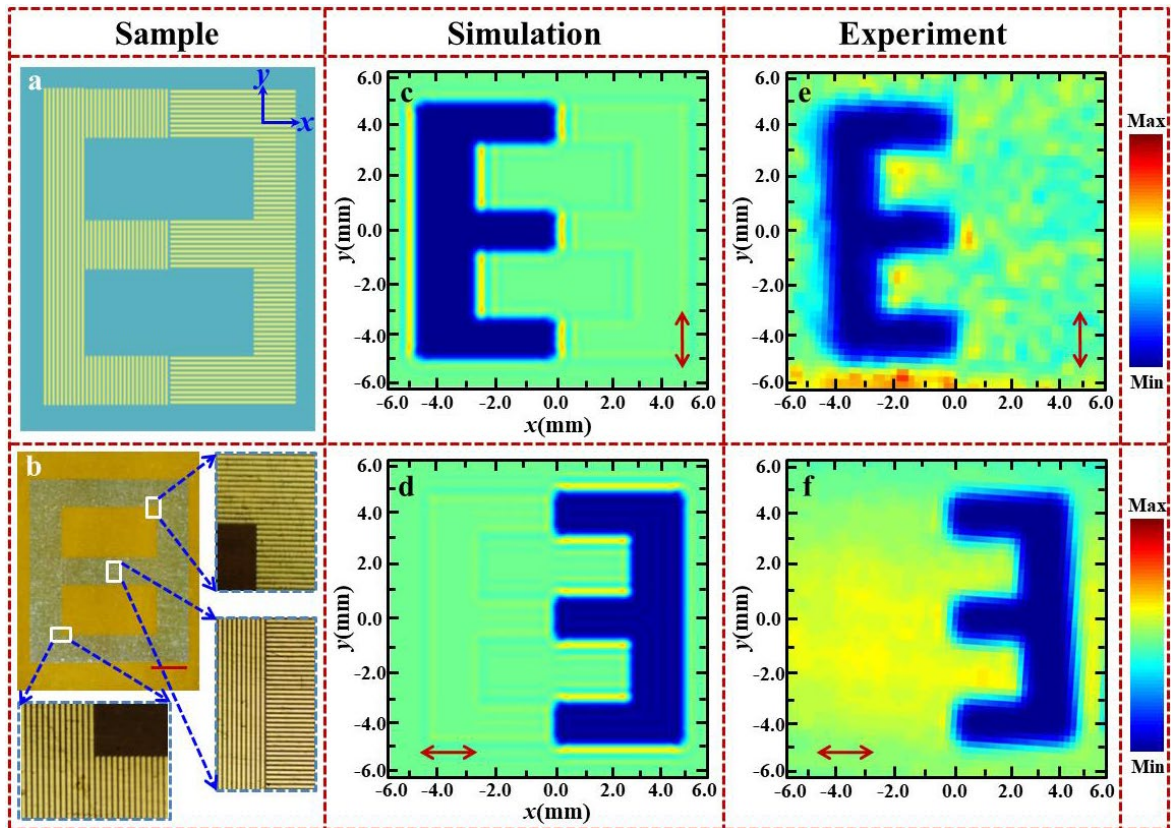
Fig.6. Polarization-dependent imaging. a and **b** The schematic and optical image of the designed sample "Sun" for polarization-dependent imaging. **c** and **d** The simulated electric field distributions for the designed imaging sample with the shinning of *x*- and *y*-polarized THz waves, respectively. **e** and **f** The measured images with the designed imaging sample inside the left and right focal spots, respectively. Here, when the designed sample "Sun" is placed in the left spot, the left "E" can be revealed by scanning the sample (the sample is continuously moved while the THz tip is fixed to record the electric field distributions), while the right "∃" can be reconstructed by the right focal spot, resulting in the polarization-dependent imaging. The red scale bar in (b) is 2mm.

A novel approach is proposed to simultaneous control of the phase and polarization in all spatial dimensions, which can enable the unprecedented capability to realize THz multi-foci metalens with polarization-rotated focal points. The simplicity and robustness of our design not only provide a platform for multiplexing of focusing and polarization rotation, but also open a novel avenue for polarization-dependent imaging.

Keyword: metasurface, metalens, polarization control, imaging

Xiaofei Zang, Hongzhen Ding, Yuttana Intaravanne, Lin Chen, Yan Peng, Jingya Xie, Qinghong Ke, Alexey. V. Balakin, Alexander. P. Shkurinov, Xianzhong Chen[*], Yiming Zhu[*], Songlin Zhuang

Title: Multi-foci metalens with polarization-rotated focal points

ToC figure
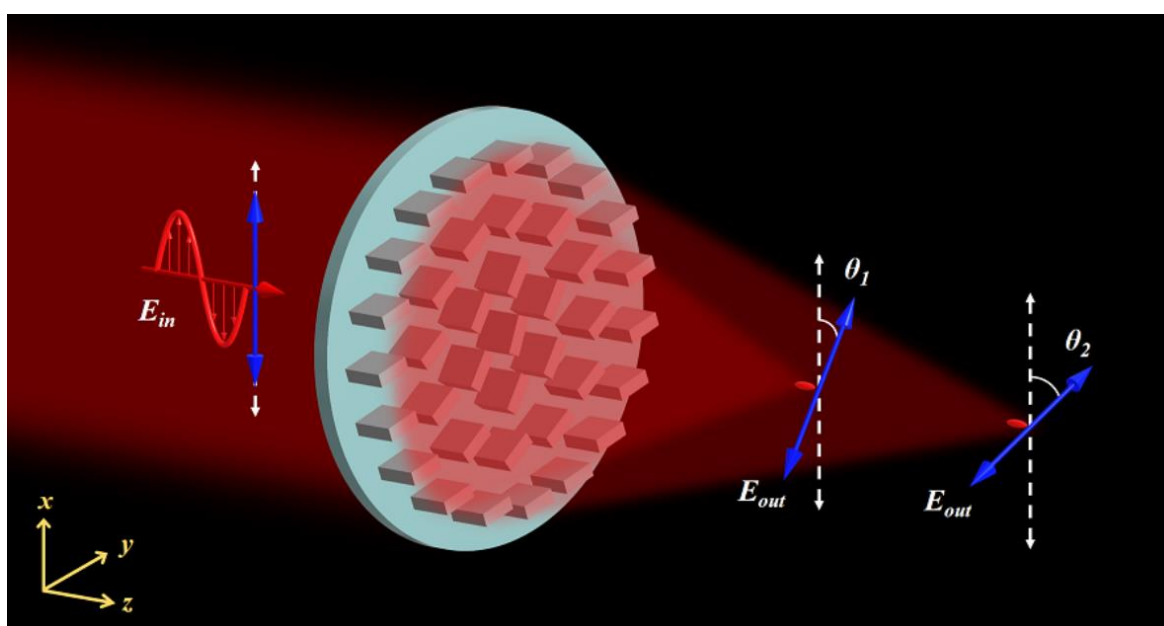
Supporting Information

Multi-foci metalens with polarization-rotated focal points

Xiaofei Zang, Hongzhen Ding, Yuttana Intaravanne, Lin Chen, Yan Peng, Jingya Xie, Qinghong Ke, Alexey. V. Balakin, Alexander. P. Shkurinov, Xianzhong Chen[*], Yiming Zhu[*], Songlin Zhuang

Supplementary Section 1. The principle of linearly-polarized multi-foci lens with functionality of polarization rotation.

The principle of linearly-polarized multi-foci lens with polarization-rotated functionality can be decomposed into five steps, as shown in the schematic of Figs. S1 and S2. Figure S1(a) shows a transmission-type of the dielectric metasurface consisting of periodic micro-pillars, in which the long axis of each anisotropic pillar is parallel to x-axis. For the normal illumination of a linearly-polarized (x-polarized) THz beam, the polarization of the transmitted beam is the same as incident THz waves. The Jones vector of the transmitted beam can be written as:

$$\begin{bmatrix} 1 \\ 0 \end{bmatrix} = \frac{1}{\sqrt{2}} \left(\frac{1}{\sqrt{2}} \begin{bmatrix} 1 \\ i \end{bmatrix} + \frac{1}{\sqrt{2}} \begin{bmatrix} 1 \\ -i \end{bmatrix} \right). \tag{1}$$

When each micro-pillar is counter-clockwise rotated with an angle of $\phi/2$, as shown in Fig. S1(b), the transmitted beam can be divided into two parts: one part is the co-polarized (non-converted) beam (the corresponding polarization is the same as the incident waves), and the other part is the polarization-rotated (converted) beam in which the corresponding polarization is modulated with a rotation angle (ϕ) with respect to the incident THz waves. Here, the polarization rotation for a linearly-polarized THz beam can be understood as follows.

The corresponding Jones matrix of a dielectric micro-pillar with rotating angle $\phi/2$ can be written as[R1]:

$$T(\varphi_1) = R(-\phi)T_0\,R(\phi)$$

$$= \begin{bmatrix} \cos(\phi/2) & -\sin(\phi/2) \\ \sin(\phi/2) & \cos(\phi/2) \end{bmatrix} \begin{bmatrix} i\sqrt{\xi(\lambda)} & 0 \\ 0 & -i\sqrt{\xi(\lambda)} \end{bmatrix} \begin{bmatrix} \cos(\phi/2) & \sin(\phi/2) \\ -\sin(\phi/2) & \cos(\phi/2) \end{bmatrix} \tag{2}$$

$$= i\sqrt{\xi(\lambda)} \begin{bmatrix} \cos(\phi) & \sin(\phi) \\ \sin(\phi) & -\cos(\phi) \end{bmatrix},$$

where T_0 and $R(\phi)$ are the Jones matrix and rotator operator of the micro-pillar, respectively.

$\xi(\lambda)$ is the conversion efficiency that can be defined as the ratio between the power with

desired polarization rotation and the incident power. A linearly-polarized THz beam along the

horizontal direction (x-axis) can be devided into two parts (LCP beam and RCP beam) with

equal intensities and the same initial phase. Upon the illumination of such linearly-polarized

THz beam, the LCP component is partially converted into RCP THz beam with an abrupt

phase delay of ϕ that is Pancharatnam-Berry phase, while the incident RCP component is

partially converted into its opposite helicity with an additional phase delay $-\phi$. The electric

field of the converted beams can be described as[R2]:

$$E_{LCP/RCP} = i\sqrt{\xi(\lambda)/2}\,e^{\mp i\phi}\begin{bmatrix} 1 \\ \pm i \end{bmatrix} \tag{3}$$

It should be noticed that the intensities of these two converted components are the same and

have the opposite helicity. Therefore, both of the converted components can be combined into

a linearly-polarized light beam with a polarization rotation of ϕ. The corresponding electric

field is expressed as follows:

$$E_{con} = i\sqrt{\xi(\lambda)/2}\,e^{-i\phi}\begin{bmatrix} 1 \\ i \end{bmatrix} + i\sqrt{\xi(\lambda)/2}\,e^{i\phi}\begin{bmatrix} 1 \\ -i \end{bmatrix} = i\sqrt{\xi(\lambda)/2}\begin{bmatrix} \cos\phi \\ \sin\phi \end{bmatrix} \tag{4}$$

As a consequence, the polarization of converted THz beam is rotated with an angle of ϕ.

If such metasurface (see as Fig. S1(b)) is introduced with an additional position dependent

phase as $\varphi = \varphi_R(x,y) = \dfrac{2\pi}{\lambda}(\sqrt{x^2 + y^2 + f^2} - |f|)$ shown in Fig. S1(c), it can focus the RCP

beam with an additional phase of $-\phi$, but defocus for the LCP beam. The Jones vector of the

converted beam under the illumination of a linearly-polarized THz beam is given as

$$i\sqrt{\xi(\lambda)/2}/\sqrt{2}\left\{\frac{1}{\sqrt{2}}\begin{bmatrix}1\\i\end{bmatrix}\exp(-i\phi)\exp(i\varphi_R(x,y))+\frac{1}{\sqrt{2}}\begin{bmatrix}1\\-i\end{bmatrix}\exp(i\phi)\exp(-i\varphi_R(x,y))\right\}$$
$$\propto\frac{1}{\sqrt{2}}\left\{\frac{1}{\sqrt{2}}\begin{bmatrix}1\\i\end{bmatrix}\exp(-i\phi)\exp(i\varphi_R(x,y))+\frac{1}{\sqrt{2}}\begin{bmatrix}1\\-i\end{bmatrix}\exp(i\phi)\exp(-i\varphi_R(x,y))\right\} \qquad (5)$$

In contrast, if we add an opposite position-dependent phase as

$\varphi'=-\varphi_R(x,y)=\varphi_L(x,y)=-\dfrac{2\pi}{\lambda}(\sqrt{x^2+y^2+f^2}-|f|)$ (f is the focal length) into the

metasurface (also see as Fig. S1(b)), as depicted in Fig. S1(d), such position-dependent phase

can focus the LCP THz beam with an additional phase of ϕ and defocus the component of the

opposite helicity. For the illumination of the linearly-polarized THz beam, the corresponding

Jones vector of the converted beam is described as

$$i\sqrt{\xi(\lambda)/2}/\sqrt{2}\left\{\frac{1}{\sqrt{2}}\begin{bmatrix}1\\i\end{bmatrix}\exp(-i\phi)\exp(i\varphi_L(x,y))+\frac{1}{\sqrt{2}}\begin{bmatrix}1\\-i\end{bmatrix}\exp(i\phi)\exp(-i\varphi_L(x,y))\right\}$$
$$\propto\frac{1}{\sqrt{2}}\left\{\frac{1}{\sqrt{2}}\begin{bmatrix}1\\i\end{bmatrix}\exp(-i\phi)\exp(i\varphi_L(x,y))+\frac{1}{\sqrt{2}}\begin{bmatrix}1\\-i\end{bmatrix}\exp(i\phi)\exp(-i\varphi_L(x,y))\right\} \qquad (6)$$

In order to obtain a linearly-polarized focal spot with polarization-rotated functionaliy(see

schematic of Fig. S1(e)), a dual position-dependent phase (both $\varphi_L(x,y)$ and $\varphi_R(x,y)$) should

be introduced, and the Jones vector is the superposition of Equations (5) and (6):

$$\frac{1}{\sqrt{2}}\left\{\frac{1}{\sqrt{2}}\begin{bmatrix}1\\i\end{bmatrix}\exp(-i\phi)\exp(i\varphi(x,y))+\frac{1}{\sqrt{2}}\begin{bmatrix}1\\-i\end{bmatrix}\exp(i\phi)\exp(-i\varphi(x,y))\right\}$$
$$+\frac{1}{\sqrt{2}}\left\{\frac{1}{\sqrt{2}}\begin{bmatrix}1\\i\end{bmatrix}\exp(-i\phi)\exp(-i\varphi(x,y))+\frac{1}{\sqrt{2}}\begin{bmatrix}1\\-i\end{bmatrix}\exp(i\phi)\exp(i\varphi(x,y))\right\}. \qquad (7)$$

The above equation can also be written as

$$\exp(i\varphi)\begin{vmatrix}\cos\phi\\\sin\phi\end{vmatrix}+\exp(-i\varphi)\begin{vmatrix}\cos\phi\\\sin\phi\end{vmatrix} \qquad (8)$$

Therefore, the required phase distribution for our proposed metalens is governed by:

$$\Phi(x, y) = \arg\left\{\exp\left[i\left(\phi + \varphi(x, y)\right)\right] + \exp\left[i\left(\phi - \varphi(x, y)\right)\right]\right\}. \tag{9}$$

Accordingly, the total phase requirement for a metalens with polarization-rotated focal spots (see schematic of Fig.1 in the main text) can be described as:

$$\begin{aligned}
\Phi_L(x, y) = \arg\Big\{ &\exp\left[i\left(\phi_1 + \varphi_1(x, y)\right)\right] + \exp\left[i\left(\phi_1 - \varphi_1(x, y)\right)\right] \\
&+ \exp\left[i\left(\phi_2 + \varphi_2(x, y)\right)\right] + \exp\left[i\left(\phi_2 - \varphi_2(x, y)\right)\right]\Big\},
\end{aligned} \tag{10}$$

where φ_1, φ_2 are the two phase profiles for the generation of two separate focal points, whose corresponding (polarization) rotation angles are represented by ϕ_1 and ϕ_2, respectively. Although both φ_1 and φ_2 are designed based on the position-dependent phase, the two focal lengths f_1 and f_2 are different.

For the transversal polarization-rotatable multi-foci metalens, the design method is slightly different from the above case. In addition to the manipulation of polarization rotation and focusing, off-axis design[R3] (see the schematic of Fig.S2) should be implemented to realize the transversal multiple focal spots. When a $\delta_x (= \pi / 7)$ phase gradient is introduced into $\pm x$ directions, the converted (focusing and polarization rotation) linearly-polarizaed THz focal spot are divided into two oblique transmitted modes with the corresponding Jones vector of

$$\frac{1}{\sqrt{2}}\left\{\frac{1}{\sqrt{2}}\begin{bmatrix}1\\i\end{bmatrix}\exp(-i\phi)\exp(i\varphi(x, y)) + \frac{1}{\sqrt{2}}\begin{bmatrix}1\\i\end{bmatrix}\exp(-i\phi)\exp(-i\varphi(x, y))\right\}\exp(i\delta_x) \quad \text{(in the right side)}$$

and $\frac{1}{\sqrt{2}}\left\{\frac{1}{\sqrt{2}}\begin{bmatrix}1\\-i\end{bmatrix}\exp(i\phi)\exp(-i\varphi(x, y)) + \frac{1}{\sqrt{2}}\begin{bmatrix}1\\-i\end{bmatrix}\exp(i\phi)\exp(i\varphi(x, y))\right\}\exp(-i\delta_x)$ (in the left side),

respectively (see Fig. S2(a)).

The corresponding Jones vector by combining the phase gradient is given as follows:

$$\begin{aligned}
&\frac{1}{\sqrt{2}}\left\{\frac{1}{\sqrt{2}}\begin{bmatrix}1\\i\end{bmatrix}\exp(-i\phi)\exp(i\varphi(x, y)) + \frac{1}{\sqrt{2}}\begin{bmatrix}1\\i\end{bmatrix}\exp(-i\phi)\exp(-i\varphi(x, y))\right\}\exp(i\delta_x) \\
&+ \frac{1}{\sqrt{2}}\left\{\frac{1}{\sqrt{2}}\begin{bmatrix}1\\-i\end{bmatrix}\exp(i\phi)\exp(-i\varphi(x, y)) + \frac{1}{\sqrt{2}}\begin{bmatrix}1\\-i\end{bmatrix}\exp(i\phi)\exp(i\varphi(x, y))\right\}\exp(-i\delta_x)
\end{aligned} \tag{11}$$

For the $-\delta_x(=-\pi/7)$ phase gradient (added in $\pm x$ directions), the converted linearly-polarized THz waves is also divided into two oblique transmitted modes, and the Jones vector is expressed as

$$\frac{1}{\sqrt{2}}\left\{\frac{1}{\sqrt{2}}\begin{bmatrix}1\\i\end{bmatrix}\exp(-i\phi)\exp(i\varphi(x,y))+\frac{1}{\sqrt{2}}\begin{bmatrix}1\\i\end{bmatrix}\exp(-i\phi)\exp(-i\varphi(x,y))\right\}\exp(-i\delta_x)$$
$$+\frac{1}{\sqrt{2}}\left\{\frac{1}{\sqrt{2}}\begin{bmatrix}1\\-i\end{bmatrix}\exp(i\phi)\exp(-i\varphi(x,y))+\frac{1}{\sqrt{2}}\begin{bmatrix}1\\-i\end{bmatrix}\exp(i\phi)\exp(i\varphi(x,y))\right\}\exp(i\delta_x)$$

(12)

In order to obtain the linearly-polarized focusing with functionality of polarization rotation in each off-axis transmitted channel (two transversal distributed focal spots, as shown in Fig. S2(c)), a dual phase-gradient ($\pm\delta_x$) should be introduced, and thus the corresponding Jones vector is the superposition of Equations (11) and (12):

$$\frac{1}{\sqrt{2}}\left\{\frac{1}{\sqrt{2}}\begin{bmatrix}1\\i\end{bmatrix}\exp(-i\phi)\exp(i\varphi(x,y))+\frac{1}{\sqrt{2}}\begin{bmatrix}1\\i\end{bmatrix}\exp(-i\phi)\exp(-i\varphi(x,y))\right\}\exp(i\delta_x)$$
$$+\frac{1}{\sqrt{2}}\left\{\frac{1}{\sqrt{2}}\begin{bmatrix}1\\-i\end{bmatrix}\exp(i\phi)\exp(-i\varphi(x,y))+\frac{1}{\sqrt{2}}\begin{bmatrix}1\\-i\end{bmatrix}\exp(i\phi)\exp(i\varphi(x,y))\right\}\exp(-i\delta_x)$$
$$+\frac{1}{\sqrt{2}}\left\{\frac{1}{\sqrt{2}}\begin{bmatrix}1\\i\end{bmatrix}\exp(-i\phi)\exp(i\varphi(x,y))+\frac{1}{\sqrt{2}}\begin{bmatrix}1\\i\end{bmatrix}\exp(-i\phi)\exp(-i\varphi(x,y))\right\}\exp(-i\delta_x)$$
$$+\frac{1}{\sqrt{2}}\left\{\frac{1}{\sqrt{2}}\begin{bmatrix}1\\-i\end{bmatrix}\exp(i\phi)\exp(-i\varphi(x,y))+\frac{1}{\sqrt{2}}\begin{bmatrix}1\\-i\end{bmatrix}\exp(i\phi)\exp(i\varphi(x,y))\right\}\exp(i\delta_x)$$
$$=\exp\{i(\varphi(x,y)+\delta_x)\}\begin{bmatrix}\cos(\phi)\\\sin(\phi)\end{bmatrix}+\exp\{i(\varphi(x,y)-\delta_x)\}\begin{bmatrix}\cos(\phi)\\\sin(\phi)\end{bmatrix}$$
$$+\exp\{i(-\varphi(x,y)+\delta_x)\}\begin{bmatrix}\cos(\phi)\\\sin(\phi)\end{bmatrix}+\exp\{-i(\varphi(x,y)+\delta_x)\}\begin{bmatrix}\cos(\phi)\\\sin(\phi)\end{bmatrix}$$

(13)

Therefore, the phase requirement for the two transversal polarization-modulated focal spots (see schematic of Fig.1 in the main text), can be written as:

$$\Phi_T(x,y)=\arg\left\{\exp\left[i(\phi+\varphi(x,y)+\delta_x)\right]+\exp\left[i(\phi+\varphi(x,y)-\delta_x)\right]\right.$$
$$\left.+\exp\left[i(\phi-\varphi(x,y)+\delta_x)\right]+\exp\left[i(\phi-\varphi(x,y)-\delta_x)\right]\right\}.$$

(14)

Supplementary Section 2. Circular-polarization insensitive metalens.

As deduced by the Equations (5) and (6), our proposed geometric metalens is insensitive of the circular-polarized THz beam, meaning that it can focus both LCP and RCP incident light beams. The numerical demonstration of such property is shown in Fig. S3. Here, the structure parameters are selected as f=6mm (focal length) and $\phi = 0^0$ (polarization rotating angle) for circular-polarization insensitive of the single focal spot. Figure S3(a) shows the electric field distribution in x-z plane of such metalens under the illumination of a LCP THz beam. One focal spot is clearly visible at z=6mm away from the surface of metalens. The corresponding electric field distribution in x-y plane at z=6mm is shown in Fig. S3(b). The polarization of the focal spot is calculated from the ellipticity that is determinated by the Stokes parameters as

$$
\begin{aligned}
S_0 &= |t_x|^2 + |t_y|^2 \\
S_1 &= |t_x|^2 - |t_y|^2 \\
S_2 &= 2|t_x||t_y|\cos(\varphi_d) \\
S_3 &= 2|t_x||t_y|\sin(\varphi_d)
\end{aligned}
\quad , \tag{15}
$$

where t_x and t_y are the transmission coefficients for x-polarized and y-polarized components. S_0 is the field intensity of output THz waves, S_1 is the linearly-polarized component along x-axis, S_2 is a linearly-polarized component in the direction of 45°, and S_3 is circularly polarized component. φ_d is the phase difference between the two orthogonal components ($\varphi_d = \varphi_{E_y} - \varphi_{E_x}$ and E_y and E_x are the two vertical components along y- and x-axis, respectively). The ellipticity of focal spot is defined as $\chi = S_3 / S_0$. As shown in Fig. S3(c), the ellipticity of focus at z=6mm is $\chi = -1$, corresponding to a RCP focal point. Similarly, under the illumination of a RCP THz beam, there is also a focal spot located at z=6mm (see Figs. S3(d) and S3(e)). In contrast, the ellipticity of such focus is $\chi = 1$ (Fig. S3(f)), resulting in a LCP focal spot. Compared with Figs. S3(a) and S3(d), it can be concluded that our designed metalenses enable the functionality of focusing that is insensitive to the incidence of both LCP and RCP THz beams. Therefore, upon the illuminate of a linearly-polarized (LP)

THz beam, a LP THz focal spot, which can be considered as the combination of both LCP and RCP components, can be realized (as demonstrated in Fig. 3 in the main text).

Supplementary Section 3. The design of the silicon pillars.

In our design of the terahertz (THz) metalens, each of the anisotropic silicon-based pillars should be optimized as a quasi-perfect half-wave plate to manipulate the wavefront of THz waves (to realize the multiple focal spots). Figure S4 shows the numerical simulation for designing such a half-wave plate (the optimized length and width of the pillar are L=85 μm, and W=40 μm while the thickness of the pillar and substrate is H=500 μm). Figure S4(a$_1$) shows the transmission spectrum of the anisotropic silicon-based pillars under the illumination of the TM (x-polarized) and TE (y-polarized) THz waves. The transmittance for both TM and TE waves are equal (T≈97%) to each other at f=0.69 THz. The phase difference between two transmitted waves is nearly π (185^0), as shown in Fig. S4(a$_2$). Therefore, the anisotropic silicon pillar has the functionality of a quasi-perfect half-wave plate at f=0.69 THz. Although the transmittance for both TM and TE waves are equal at other frequencies, *i.e.*, 0.35, 0.43, 0.52, 0.6 THz, the phase differences are largely deflected from π, leading to a non-perfect half-wave plate. We further demonstrate the function (half-wave plate) of silicon pillars at f=0.69 THz, as shown in Figs. S4(b) and S4(c). For the incidence of LCP THz waves, the numerical value of the phase shift (Pancharatnam-Berry phase) for the transmitted RCP (cross-polarized) waves is equal to twice the rotation angle of the unit cell and the transmittance for each rotation angle is nearly equal, leading to a quasi-perfect half-wave plate (Fig. S4(b)). In addition, the transmitted THz wave with the inverse spin has a tilted wavefront as shown in Figs. S4(c$_1$) and S4(c$_2$), demonstrating a gradient phase shifting by the silicon pillars.

Supplementary Section 4. Electric field distributions for metalens with one focal spot

Figure S5 shows the numerical calculation and experimental demonstration of the characteristics for the linearly-polarized and polarization-rotatable metalens (also see the schematic of Fig. S5(a)). Under the illumination of *x*-polarized THz waves, a focal spot is formed at *z*=6mm. Compared with Figs. S5(b) and S5(c), it can be found that the *x*-polarized THz waves is converted into a *y*-polarized focal spot with polarization rotation of 90^0. Figures S5(d) and S5(e) also show the measured electric field distributions in the *y*-*z* plane. It is experimentally demonstrated that the incident THz waves is focused into a focal spot nearly at *z*=6mm with polarization rotation of 90^0 as illustrated in Fig. S5(d), and none of the *x*-polarized electric field contributes to the focal spot (see Fig. S5(e)).

Supplementary Section 5. Electric field distributions for longitudinal multi-foci metalens and focusing properties (amplitude information)

Longitudinal multi-foci metalens with polarization rotation is shown in Fig. S6. For the incidence of *x*-polarized THz beam, there are two longitudinal distributed focal spots observed at *z*=3mm and *z*=6mm, respectively (see *y*-*z* plane of the electric field distributions in Fig. S6(a) and S6(b)). The polarizations of these two focal spots are orthogonal with each other that are polarized along *y*-axis for the left spot and *x*-axis for the right one. The experimental demonstrations of the above properties are illustrated in Figs. S6(c) and S5(d). In addition, the *x*-*y* plane of electric field distributions are also calculated and measured in Figs S6(e)~S6(h). It can be concluded that none of the *x*-polarized and *y*-polarized electric fields is detected from the left and right focal spots.

The focusing properties (amplitude information) of the longitudinal multiple focal spots are shown in Fig. S7. Fig S7(a) shows the numerical and experimental intensity curves ($|E_y|^2$) of the left focus spot at *z*=3mm and *y*=0mm, while the corresponding intensity distributions of $|E_x|^2$ are illustrated in Fig. S7(b). In comparison with Figs. S7(a) and S7(b), only *y*-polarized focal spot is formed at *z*=3mm. In contrast, the focal spot at *z*=6mm is *x*-polarized, as shown

in Figs. S7(c) and S7(d). In addition, as shown in Fig. 7, the metalens has the capability of focusing (with longitudinal dual-focal spots) close to the numerical excepted values except for a slight discrepancy, which can be attributed to the sample imperfection and the limited number of micro-pillars in metalens.

Supplementary Section 6. Electric field distributions for transversal multi-foci metalens

The schematic of the transversal multi-foci metalens with functionality of polarization rotation is shown in Fig. S8(a). Here, the basic principle for such metalens is depicted in section 1 and the polarization rotating angle is selected as $\phi = 90^0$. As shown in Figs. S8(b) and S8(c), the *x*-polarizaed incidence of THz waves is focused and splitted into two transversal distributed focal spots located at (±2mm, 0, 5mm). The polarizations of both spots are rotated with 90 degree with respect to the incident THz waves, and only *y*-polarized focal spots are detected (see Figs. S8(d) and S8(e)). Figures S8(f)～S8(i) show the measured results of such metalens, and they also demonstrated the properties of two transversal distributed focal points with the polarization rotation. The characteristics of focusing and polarization rotating for the designed metalens are also demonstrated with *x-y* plane of electric distributions, as shown in Figs. S8(f)～S8(i), respectively.

Supplementary Section 7. Transmission spectra of the metal-based slits

To simultaneously characterize the lens imaging functionality and polarization-rotated capability, a polarization-dependent sample, named Chinese character "Sun" with bilateral symmetry, is designed for imaging (see Fig 9(a) in main text). The proposed design consists of periodic arranged metal-based slits coating on the PI (polyimide) substrate (also see Fig 9(b) in main text). There are four types of the slits are required to design the sample, as shown in Fig.S9. It can be seen that the transmission of all metal-slits is over than 93% (at 0.69 THz) when the polarization of the incident THz waves is perpendicular to the long-axis of the slits.

However, it is lower than 8% (nearly blocked) when the polarization of the incident THz waves is parallel to the long-axis of the slits. Therefore, for the two orthogonal arranged slit arrays, it is hypersensitive to the polarization of the incident THz waves, which can be applied for the polarization-dependent imaging.

Supplementary Section 8. Polarization conversion efficiency and focusing efficiency of the designed metalens

Polarization conversion efficiency is one of the key aspect in the performance of designed metalens. Here, the polarization conversion efficiency is defined as the ratio between the power of desired polarization rotation and incident power, similar to that in Ref [R4] (each micro-pillar is considered as a half wave plate that rotates the polarization of linearly-polarized light with rotating angle of 2θ, where θ is the angle between the long side of micro-pillar and the plane of polarization). In theory, the polarization rotated (or converted) component is directly related to the focal spots, as shown in Eqs (4)~(14). In the meantime, it is difficult to measure the efficiency of the focal spots with the NSTM (near-field scanning terahertz microscopy). Therefore, the polarization conversion efficiency of the polarization rotated/converted component can reveal the performance of the designed metalens. To achieve the polarization conversion efficiency of the anistropic pillar, uniform array of micro-pillars are fabricated and the orientation of each pillar is rotated counter-clockwise with an angle of 45^0. Consequently, the incidence of x-polarized THz beam is partially converted into the beam with polarization along y-direction. The polarization conversion efficiency of the micro-pillar array is the ratio between the power of y-polarized beam and incident power. As shown in Fig. S9, the polarization conversion efficiency are 97% (Fig. S10(a)) for numerical calculation and nearly 45% (Fig. S10(b)) for the measurement at 0.69 THz. The strong oscillations in efficiency can be qualitatively explained as the Fabry-Perot resonance, like in

Ref [R5]. The polarization conversion efficiency for measurement is lower than that for the numerical simulation which can be due to the fabrication errors.

Figure S11(a) shows the polarization conversion efficiency under the influence of height of the anisotropic silicon pillar. When the height of the silicon pillar changed from 450μm to 550μm (the length and width of the pillar are 85μm and 40μm, respectively), the resonance frequencies and the corresponding polarization conversion efficiencies are variable with diferent heights of the pillar. For example, the polarization conversion efficiencies at 0.69 THz are 56%, 98% and 44% for H=450μm, 500μm, and 550μm, respectively. The influence of the length for the polarization conversion efficiency (the height and width of the pillar is 500μm and 40μm, respectively) is illustrated in Fig. S11(b). When the length of the silicon pillar is varied from 80 to 90μm, the primary influence is on the polarization conversion efficiencies while the resonance frequencies are almost unaffected. For changing of the width of the silicon pillar, both the resonance frequencies and the corresponding polarization conversion efficiencies are almost unaffected, as shown in Fig.S11(c). From the above discussion, we can conclude that the height and the length of the silicon pillar are main factors that determinate the resonance frequency and polarization conversion efficiency. Therefore, the measured polarization conversion efficiency only half of the theoretically predicted value can be attributed to the fabrication tolerances/errors (especially the height tolerances of the silicon pillar). Furthermore, the different period of this oscillation different between the simulation and the experiment can also be attributed to the fabrication tolerances/errors.

The numerical simulations for the focusing efficiency are shown in Table I. For the single focusing with polarization-rotated functionality (rotation angle of 90^0), the focusing efficiency is 31.5%, while it is 32.5% for the longitudinal dual-focal spots. In addition, the focusing efficiencies for the transverse focal spots without and with polarization rotating are 32% and 30%, respectively. It should be noticed that the performance of metalens with the target phase profile shown in Eq.9 is implemented purely by geometric phase nanostructures. The target

phase of in Eq.9 consists of the phase profile of a convex lens and a concave lens (resulting in diverging beam). Therefore, under the illumination of LCP THz waves, just half of the transmitted waves will be converted to RCP light with an additional phase delay of ϕ. In contrast, for the RCP incidence, half of the transmitted waves will be converted to LCP light with an additional phase delay of $-\phi$. Here, only half (in theory) of the transmitted THz waves converted to RCP/LCP light is attributed to the phase profile of a convex lens $exp(\varphi)$ and a concave lens $exp(-\varphi)$ (resulting in divergent beam) in Eq.4. Since a linearly-polarized light beam can be considered as the superposition of both LCP and RCP components with the equal amplitudes, a metalens with the phase profile shown in Eq.4 can generate a linearly-polarized focal point with polarization-rotated functionality (with rotating angle of $\pm\phi$) under the illuminate of linearly-polarized light. Therefore, for the linearly-polarized incidence, the maximal focusing efficiency cannot exceed 50% in theory. All of the numerical simulations for focusing efficiency are nearly by the 31.5%, which is in agreement with the theoretical prediction ($\leq$50%). As shown in the main text, Eq.5 and Eq.6 illustrate the target phase profiles for the longitudinal and transverse focal spots, respectively. In each equation, the first two items show the phase profile for the left (up) focal spot, while the latter two items depict the phase profile for the right (down) focal spot. It should be pointed out that the amplitude of each item in Eq.10 and Eq.14 is equal, which means that the efficiencies of metalens with the two focal spots are equal in theory. However, for the longitudinal multi-foci metalens, the efficiency for the left focusing is 17.5%, but 15% for the right one. The slight discrepancy may be attributed to finite silicon pillars (100×100) in numerical simulations, different focusing distance and numerical aperture for the focal spots.

TABLE I Focusing efficiency of the designed metalenses

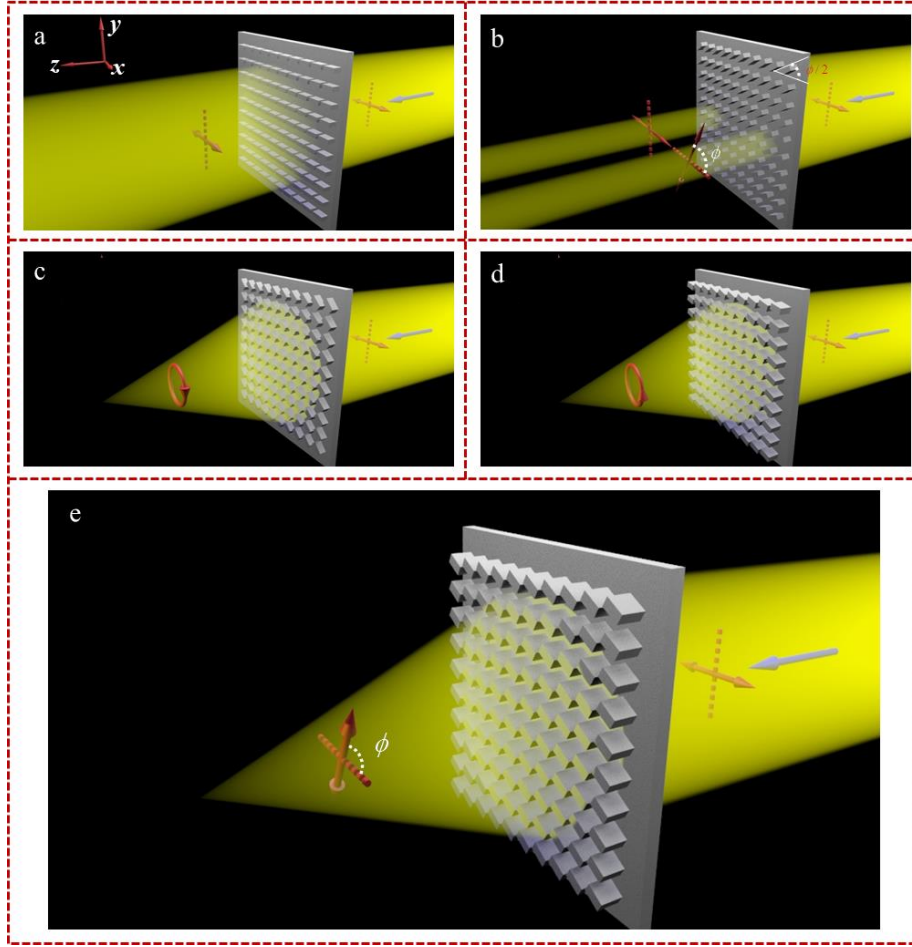| Focusing efficiency			
Single foci with polarization rotation	**longitudinal multiple focal spots**	**Transversely focis without polarization rotation**	**Transversely focis with polarization rotation**
31.5%	32.5%	32%	30%

Fig. S1 Schematic of the linearly-polarized and polarization-rotatable focusing: **a)** for the horizontal arranged rod array; **b)** each rod rotated with an angle of $\varphi/2$; **c)** for the case of adding position dependent phase as $\varphi = \varphi_R(x,y) = \dfrac{2\pi}{\lambda}(\sqrt{x^2 + y^2 + f^2} - |f|)$; **d)** for the case of adding position dependent phase as $\varphi = -\varphi_R(x,y) = -\dfrac{2\pi}{\lambda}(\sqrt{x^2 + y^2 + f^2} - |f|)$; **e)** the metasurface-based linearly-polarized focusing with polarization-rotation.
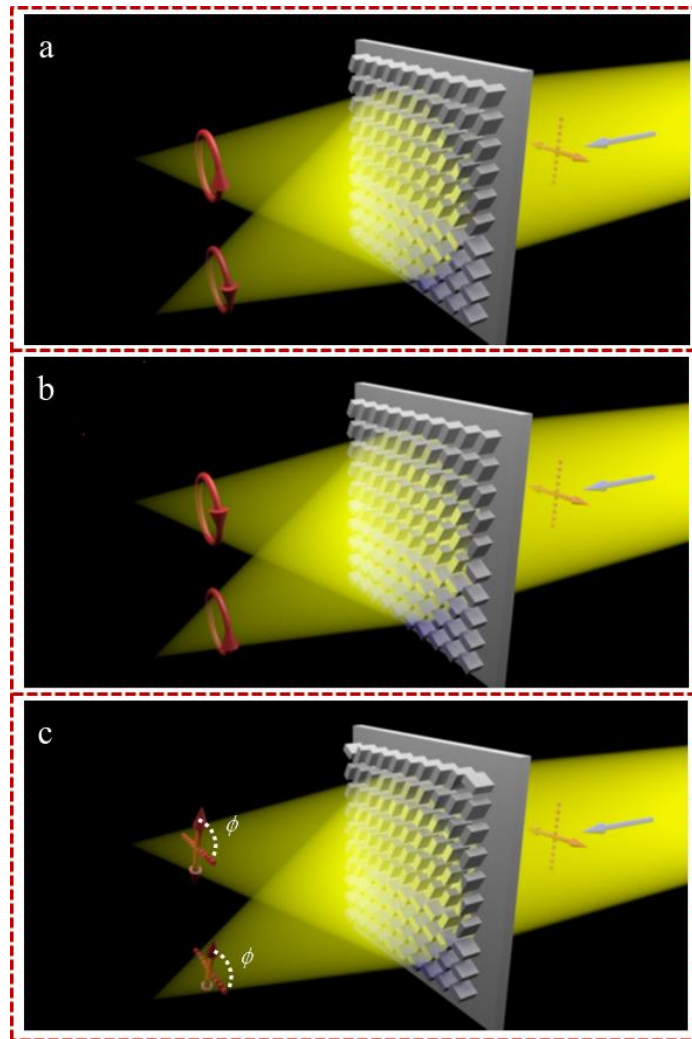
Fig. S2 Schematic of the off-axis for transverse multi-foci metalens: **a)** for case of adding the $\delta_x = (\pi/7)$ phase gradient in $\pm x$-directions; **b)** for case of adding the $-\delta_x = (-\pi/7)$ phase gradient in $\pm x$-directions; **c)** the metasurface-based transverse dual-foci THz metalens.
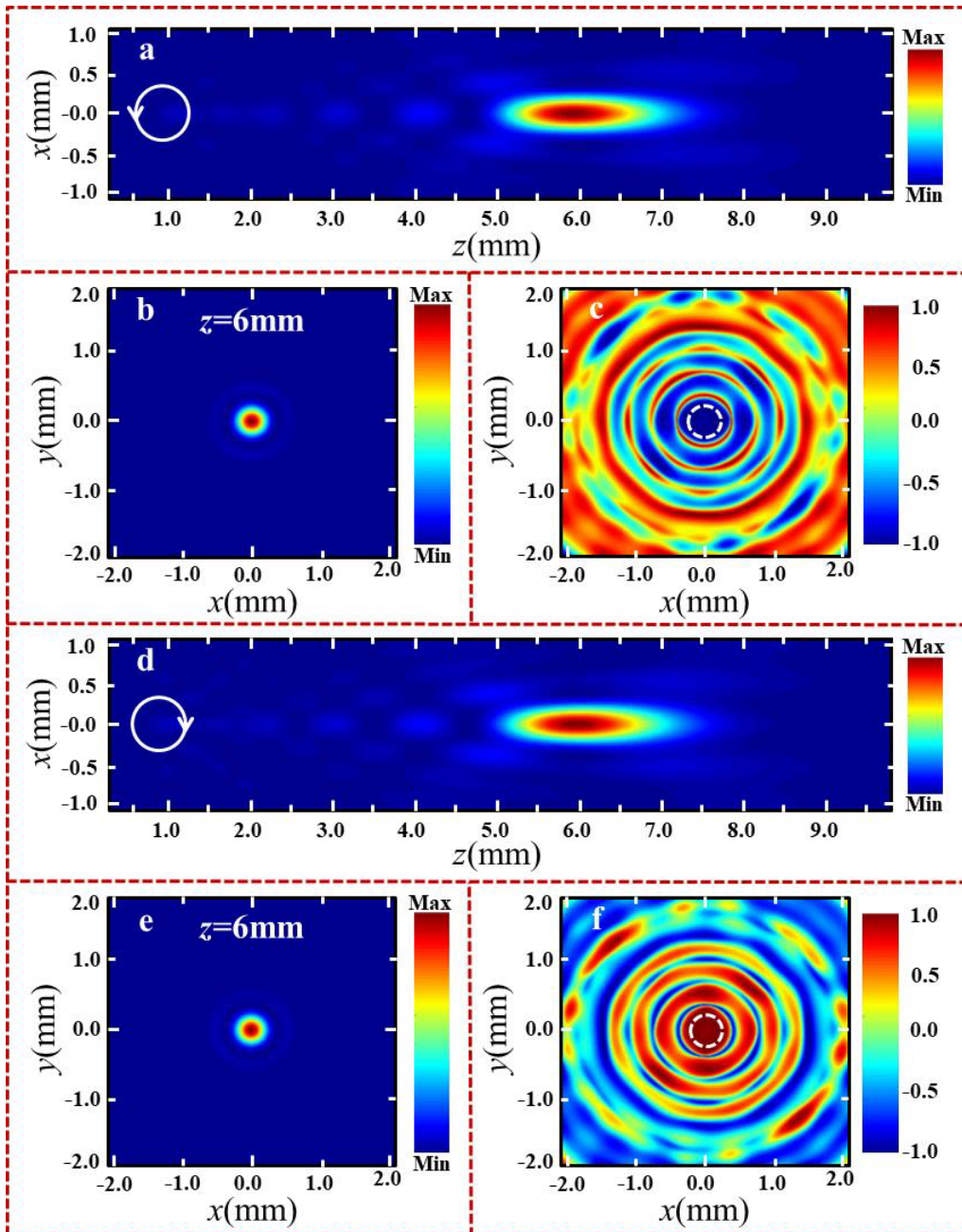
Fig. S3 Electric field distributions and ellipticity of the circular-polarization insensitive metalens: **a)** the electric field distribution of the meatlens in *x-z* plane under the illumination of left-hand circular-polarized THz waves at 0.69 THz; **b)** and **c)** the corresponding electric field distribution and ellipticity in *x-y* plane (at *z*=6 mm). **d)** the electric field distribution of the meatlens in *x-z* plane under the illumination of right-hand circular-polarized THz waves at 0.69 THz; **e)** and **f)** the corresponding electric field distribution and ellipticity in *x-y* plane (at *z*=6 mm).
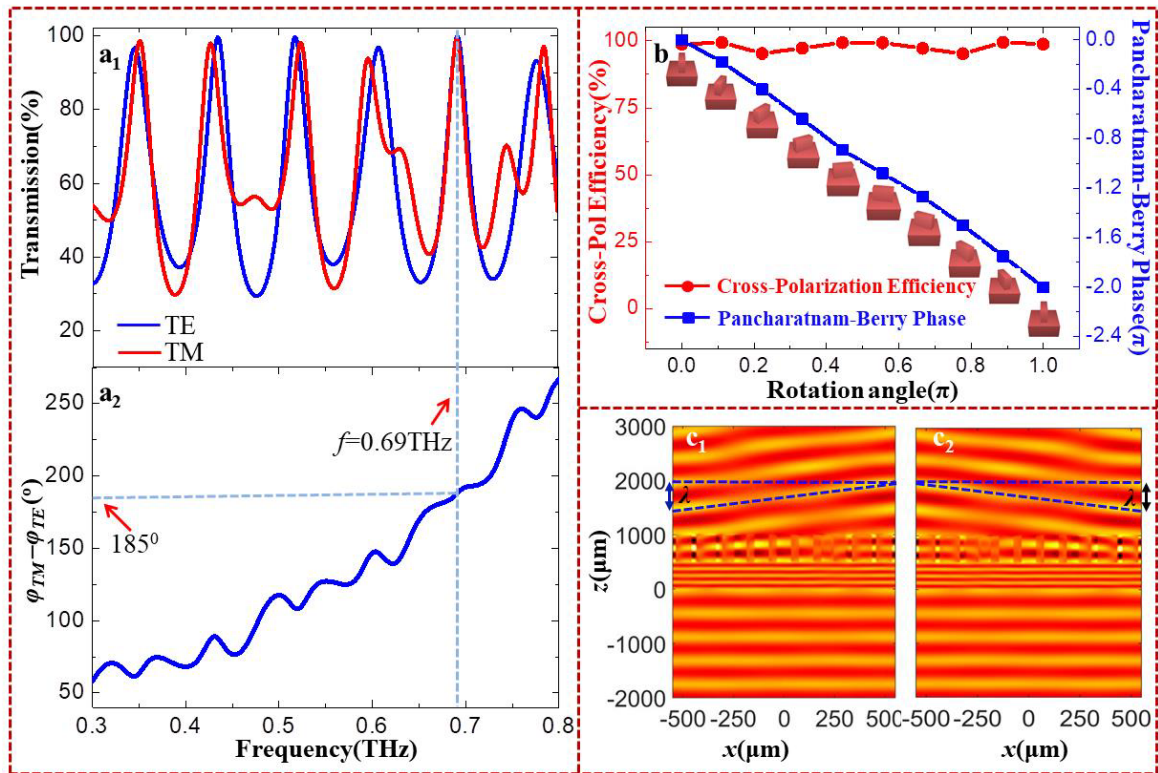
Fig. S4. The design of the silicon pillars. a₁) The transmittance of the silicon pillars under the illumination of TM (red) and TE (blue) THz waves. **a₂)** The phase difference between the transmitted TE and TM waves. **b)** The transmittance and phase shift of the silicon pillar with different rotation angles. **c₁)** and **c₂)** Electric field distributions of the transmitted THz waves with LCP (c₁) and RCP (c₂) incidence through a periodic array with rotation angle varying from 0 to 160⁰ with an equal interval of 20⁰.
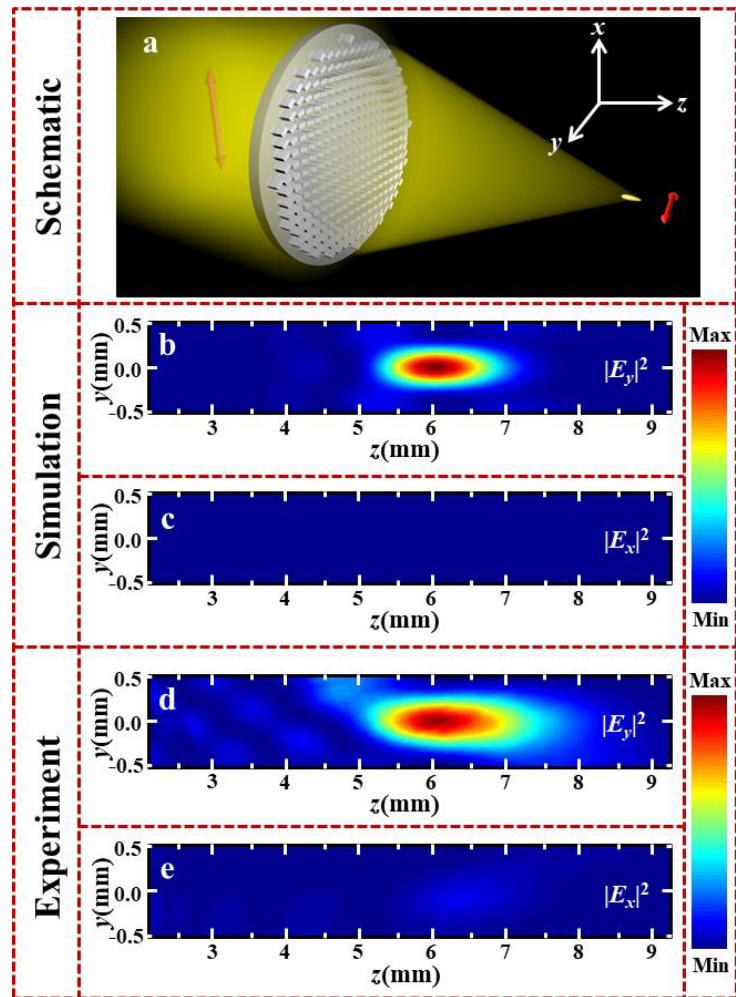
Fig. S5 Schematic and electric field distributions for the polarization-rotatable of single-foci metalens under the illumination of *x*-polarized THz waves: **a)** the schematic of the designed metalens; **b)** and **c)** the simulated *y*- and *x*-polarized electric field distributions for the transmitted THz waves at *y*-*z* plane; **d)** and **e)** the corresponding measurements for the polarization-rotatable of single-foci metalens.
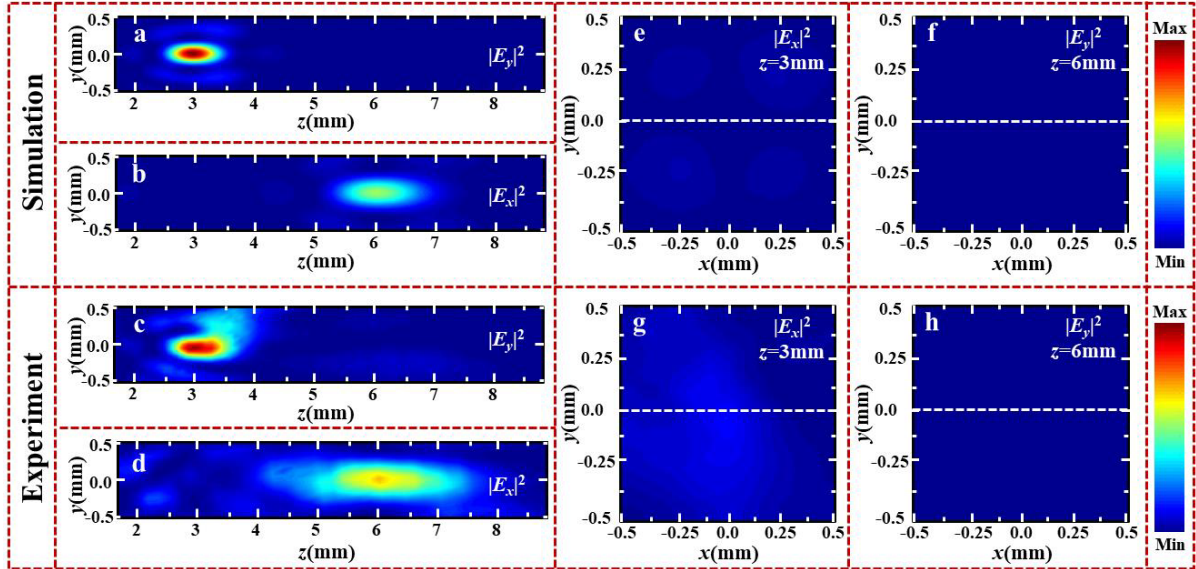
Fig. S6 Electric field distributions for the polarization-rotatable of longitudinal multi-foci metalens under the illumination of *x*-polarized THz waves: **a)** and **b)** the simulated *y*- and *x*-polarized electric field distributions for the transmitted THz waves at *y*-*z* plane. **c)** and **d)** the corresponding measurments for the polarization-rotatable of dual-foci metalens. **E)** and **f)** The simulated electric field distributions for the designed metalens at *x*-*y* plane and *z*=3mm, *z*=6mm, respectively. **g)** and **h)** The corresponding measurments for the designed metalens at *x*-*y* plane and *z*=3mm, *z*=6mm, respectively.
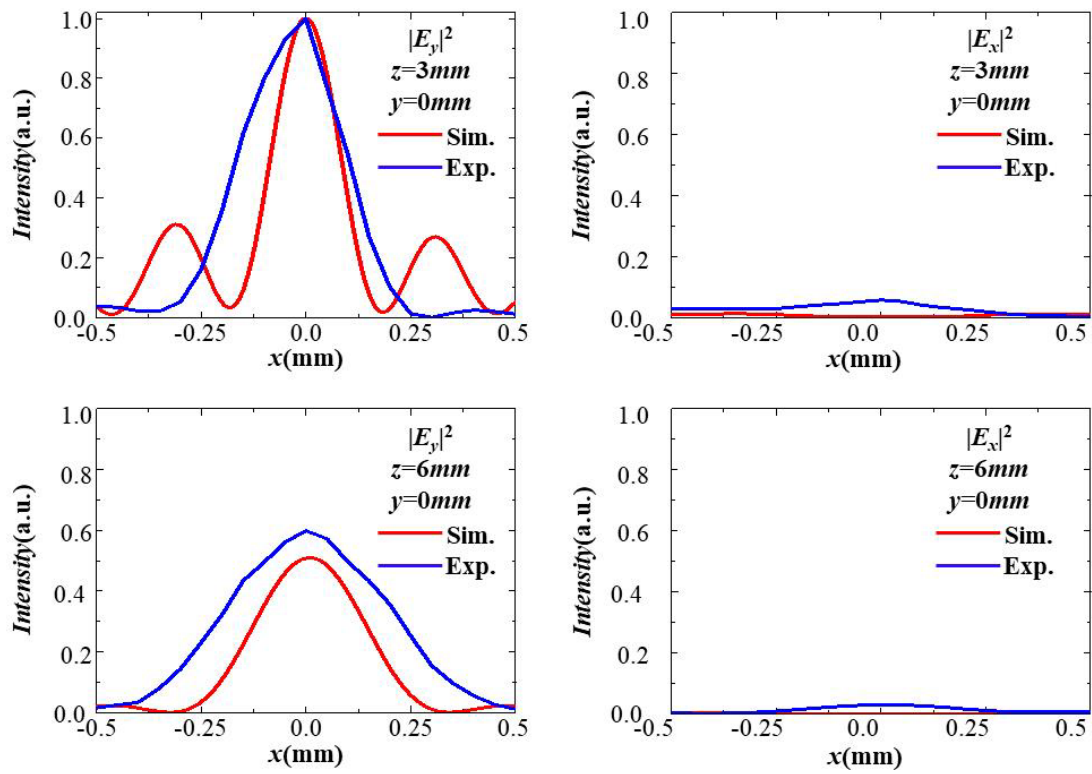
Fig. S7 Comparison of the numerical and experimental focusing properties (amplitude information) at the focal plane: **a)** z=3mm, y=0mm for the $|E_y|^2$; **b)** z=3mm, y=0mm for the $|E_x|^2$; **c)** z=6mm, y=0mm for the $|E_x|^2$; **d)** z=6mm, y=0mm for the $|E_y|^2$.
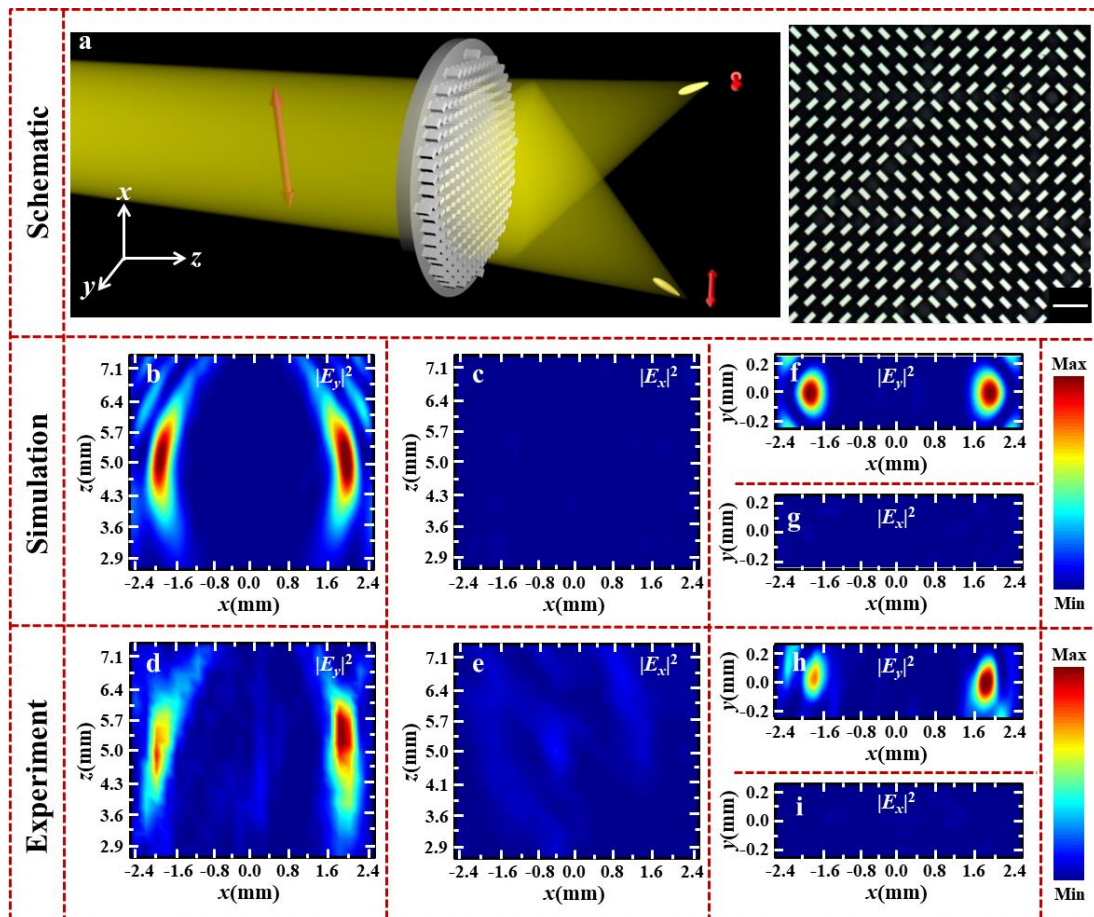
Fig. S8 Schematic and electric field distributions for the polarization-rotatable of transverse multi-foci metalens under the illumination of *x*-polarized THz waves. a) the schematic and fabricated sample for polarization-rotatable of the transverse dual-foci metalens. **b)** and **c)** the simulated *x*- and *y*-polarized electric field distributions for the transmitted THz waves at *x-z* plane. **d)** and **e)** The corresponding measurments for the polarization-rotatable of transverse dual-foci metalens. **f)** and **g)** The simulated electric field distributions for the designed metalens at *x-y* plane and *z*=5mm, respectively. **h)** and **i)** the corresponding measurments for the designed metalens at *x-y* plane and *z*=5mm, respectively. The scale bar is 200μm.
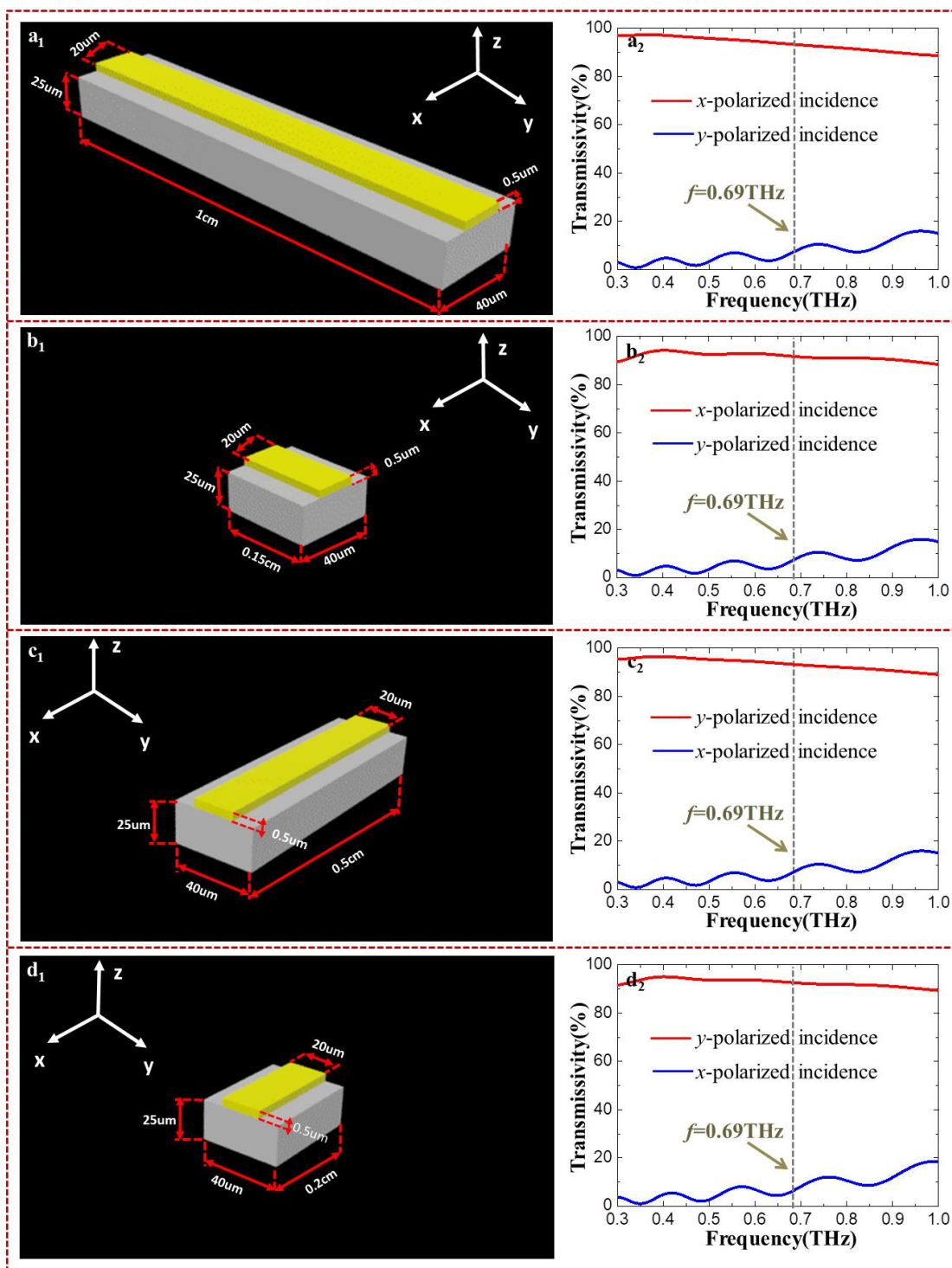
Fig. S9 Schematics and transmission spectra of the metal-based slits: a₁)～d₁) the unit

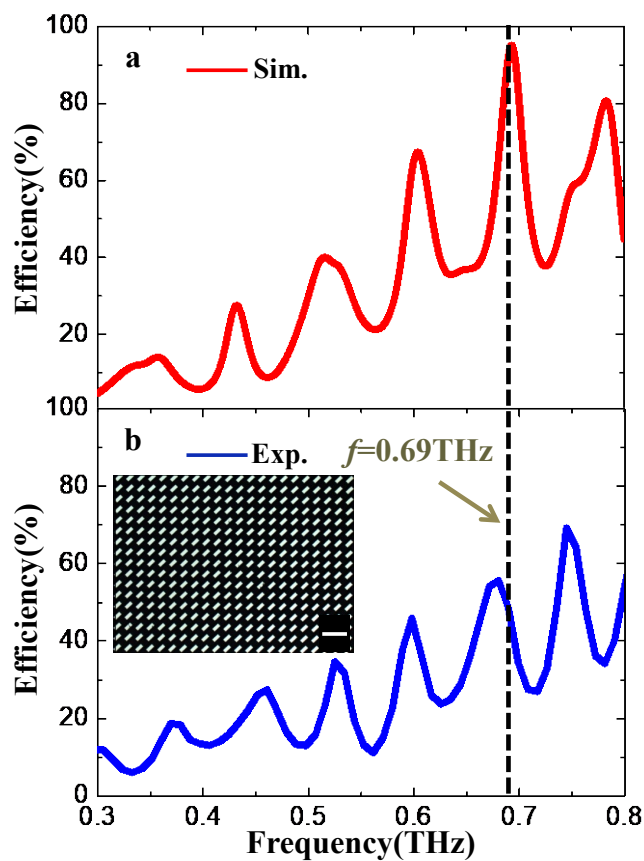cell of the four metal-based slits; **a₂)～d₂)** the corresponding transmission spectra.

Fig. S10 The polarization conversion efficiency for the micro-pillars: a) the simulated polarization conversion efficiency; **b)** the measured polarization conversion efficiency and the fabricated sample. The scale bar is 200μm. Inset is the fabricated sample for measuring the polarization conversion efficiency.
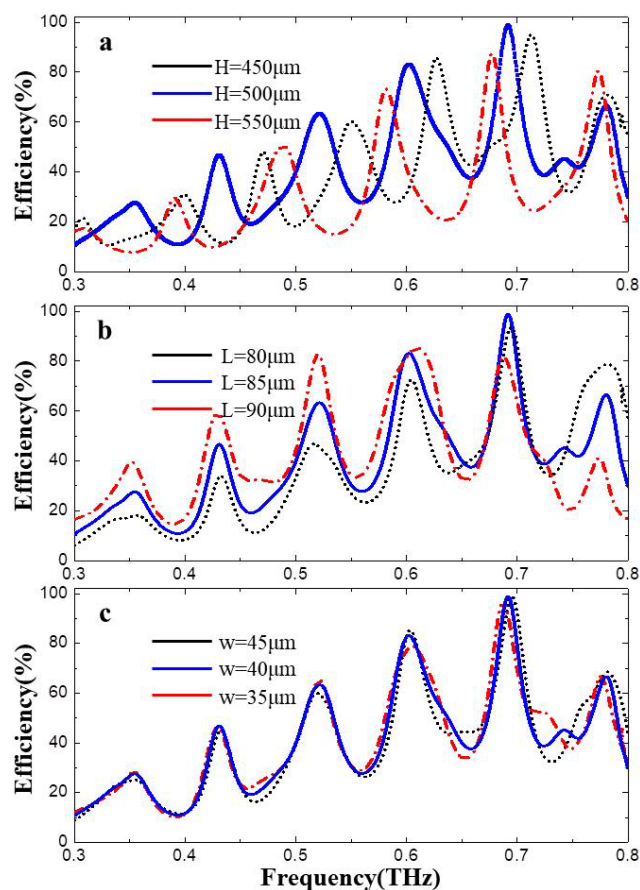
Fig. S11. The dependence of polarization conversion efficiency of the silicon posts on structure parameters. **a)**The polarization conversion efficiencies for different height of the silicon pillar; **b)**The polarization conversion efficiencies for different lengths of the silicon pillar; **c)** The polarization conversion efficiencies for different widths of the silicon pillar.

References

R1. D.Goldstein, D. Polarized light (*Marcel Dekker*, 2003).

R2. K. Huang, Z. Dong, S. Mei, L. Zhang, Y. Liu, H. Liu, H. Zhu, J. Teng, B. Lukyanchuk, J. Yang, C. Qiu. *Laser Photon. Rev.* **2016**, 10, 50.

R3. F. Yue, C. Zhang, X. Zang, D. Wen, B. Gerardot, S. Zhang, X. Chen, *Light: Sci & Appl.* **2018**, **7**, 17129.

R4. X. Zang, F. Dong, F. Yue, C. Zhang, L. Xu, Z. Song, M. Chen, P. Chen, G. S. Buller, Y. Zhu, S. Zhuang, W. Chu, S. Zhang, X. Chen. *Adv. .Mater.* **2018**, 30, 1707499.

R5. A. Arbabi, Y. Horie, M. Bagheri, A. Faraon. *Nature Natecnnol.* **2015**, 10, 937.